Научная статья

УДК 528.88 + 551.463 + 556.5
DOI: 10.24412/2658-4255-2022-2-44-71

Для цитирования:
V. V. Tikhonov, A. N. Romanov, I. V. Khvostov, T. A. Alekseeva, A. I. Sinitskiy, M. V. Tikhonova, E. A. Sharkov, N. Yu. Komarova Analysis of the hydrological regime of the Gulf of Ob in the freezing period using SMOS data // Российская Арктика. 2022. № 17. С. 44–71

Получена: 19.07.2022
Принята: 23.07.2022
Опубликована: 27.07.2022

Funding. This study was supported by the Russian Foundation for Basic Research (project No. 20-05-00198a) (V.V. Tikhonov, I.V. Khvostov, A.N. Romanov, A.I. Sinitsky, N.Yu. Komarova). Modeling of microwave radiation of the Arctic Sea ice was carried out in the framework of the "Monitoring" State Research Theme (State Reg. No. 122042500031-8) (T.A. Alexeeva, E.A. Sharkov).
Финансирование. Работа выполнена при поддержке РФФИ (проект № 20-05-00198а) (Тихонов В.В., Хвостов И.В., Романов А.Н., Синицкий А.И., Комарова Н.Ю.). Моделирование микроволнового излучения арктического морского льда проводилось в рамках государственной научно-исследовательской темы "Мониторинг" (гос. рег. № 122042500031-8) (Т.А. Алексеева, Е.А. Шарков).

ANALYSIS OF THE HYDROLOGICAL REGIME OF THE GULF OF OB IN THE FREEZING PERIOD USING SMOS DATA

V. V. Tikhonov[1,2*], A. N. Romanov[2], I. V. Khvostov[2], T. A. Alekseeva[3,1], A. I. Sinitskiy[4], M. V. Tikhonova[5], E. A. Sharkov[1], N. Yu. Komarova[1]

[1] Space Research Institute of the Russian Academy of Sciences, Moscow, Russia
[2] Institute for Water and Environmental Problems of the Siberian Branch of the Russian Academy of Sciences, Barnaul, Russia
[3] Arctic and Antarctic Research Institute, St. Petersburg, Russia
[4] "GEOINGSERVICE", LLP, Moscow, Russia
[5] Russian State Agrarian University — Moscow Timiryazev Agricultural Academy, Moscow, Russia
* vtikhonov@asp.iki.rssi.ru

Abstract. The Gulf of Ob is a unique ecosystem characterized by a complex interaction of river and sea factors. It is exposed to extremely strong seasonal pressure of highly variable temperature, insolation, biogenic load and many other factors, including anthropogenic and technogenic effects. Operational satellite data on the hydrological regime of the Gulf of Ob are crucial for the analysis of different environmental and climate processes as well as assessment of the intensity and scale of anthropogenic and technogenic impacts on the adjacent areas. This study presents an analysis of seasonal and interannual variations of brightness temperature in different parts of the Gulf of Ob in the freezing period based on SMOS (Soil Moisture and Ocean Salinity) data. It was found that in the southern part of the Gulf of Ob, the seasonal and interannual brightness temperature dynamics are similar to freshwater lakes. However, the closer to the Kara Sea the more these dynamics deteriorate and, finally, in the northern part of the Gulf, become similar to those of the central Kara Sea. During the freezing period, changes in the brightness temperature dynamics occur in different parts of the Gulf of Ob. This is explained by an increase in the salinity of water under ice. It was shown that during winter seasons, the zone of fresh and salt waters mixing (the transition zone) can shift far to the south of the Gulf of Ob. Winter shift of the transition zone was compared with climate changes in the region that determine the river runoff and the state of permafrost. The revealed patterns of brightness temperature seasonal variations in different parts of the Gulf of Ob and the associated ice cover phases can be used to assess the hydrological regime in large estuaries of the Arctic in winter, as well as climate changes in the adjacent areas on the basis of satellite microwave radiometry data.

Keywords: microwave radiometry, SMOS, estuary, ice cover, fresh and salt waters mixing zone

АНАЛИЗ ГИДРОЛОГИЧЕСКОГО РЕЖИМА ОБСКОЙ ГУБЫ В ПЕРИОД ЛЕДОСТАВА ПО ДАННЫМ SMOS

В. В. Тихонов[1,2,*], А. Н. Романов[2], И. В. Хвостов[2], Т. А. Алексеева[3,1], А. И. Синицкий[4], М. В. Тихонова[5], Е. А. Шарков[1], Н. Ю. Комарова[1]

[1] Институт космических исследований РАН, Москва, Россия
[2] Институт водных и экологических проблем СО РАН, Барнаул, Россия
[3] Институт водных и экологических проблем СО РАН, Барнаул, Россия
[4] ООО «ГЕОИНЖСЕРВИС», Москва, Россия

[5] Российский Государственный Аграрный Университет - МСХА имени К.А.Тимирязева, Москва, Россия
* vtikhonov@asp.iki.rssi.ru

Аннотация. Обская губа представляет собой уникальную экосистему, находящуюся в условиях сложного взаимодействия речных и морских факторов. Она подвержена очень сильным сезонным воздействиям с существенными колебаниями температуры, солнечной освещённости, биогенной нагрузки и множеством других факторов, включая антропогенные и техногенные воздействия. Оперативные спутниковые данные о гидрологическом режиме Обской губы являются важнейшим источником информации для анализа различных природных и климатических процессов, а также оценки интенсивности и мощности антропогенного и техногенного воздействия на прилегающие территории. В этом исследовании представлен анализ сезонных и межгодовых зависимостей яркостной температуры различных областей Обской губы в период ледостава, полученных по данным спутника SMOS (Soil Moisture and Ocean Salinity). Проведенные исследования показали, что в южной части Обской губы наблюдается схожая с пресноводными озерами сезонная и межгодовая динамика яркостной температуры. Однако, ближе к акватории Карского моря эта динамика нарушается и в северной части губы становится схожей с динамикой яркостной температуры центральной области Карского моря. Изменение сезонной динамики яркостной температуры различных областей Обской губы происходит в период ледостава. Такое изменение объясняется увеличением солености воды подо льдом. Проведенные исследования показали, что в зимние сезоны область смешения пресных и соленых вод (фронтальная зона) может сдвигаться далеко на юг Обской губы. Смещение фронтальной зоны в зимний период сопоставлено с климатическими изменениями региона, определяющими речной сток и состояние многолетнемерзлых пород. Выявленные закономерности сезонных вариаций яркостной температуры различных участков Обской губы и связанные с ними фазы ледяного покрова могут быть использованы для оценки гидрологического режима в крупных эстуариях Арктики в зимнее время, а также климатических изменений прилегающих территорий по данным спутниковой микроволновой радиометрии.

Ключевые слова: микроволновая радиометрия, SMOS, эстуарий, ледяной покров, зона смешения пресных и соленых вод

INTRODUCTION

Notable changes in the state and dynamics of various climate and hydrological processes have been recorded in the Arctic. These include: an increase in average air temperature; a reduction in duration of snow cover season; late ice formation and early opening of river, lake and sea ice; increased freshwater runoff; glacier melt; degradation of permafrost; reduction in sea ice area, etc. [1]. These changes also affect numerous rivers flowing into the Arctic Ocean. Among them are four of the twelve longest rivers on Earth, namely Yenisei, Ob, Lena, and Mackenzie [2-6]. These rivers account for nearly 60% of the freshwater that flows from the continents into the Arctic Ocean. Because of its unique land-sea connection, the Arctic Ocean is exposed to greater inflow of freshwater than any other ocean [7].

The Arctic River deltas and estuaries are unique ecosystems involved in complex interaction of river and sea factors. They are characterized by considerable variability and high ecological vulnerability. At the same time, however, they possess significant natural resources that play an important role in the economy of coastal regions [8-10]. Globally, areas of mixing sea and river waters represent an ocean "filter" belt. The effectiveness of such a "filter" in shallow waters is much higher than in the open ocean. One of the important aspects in the study of brackish waters is establishing and refining the dependencies of various processes on salinity of mixing sea and fresh waters [11, 12]. The Arctic estuaries are subject to very strong seasonal influences with significant variations in temperature, insolation, ice cover, snow water equivalent, biogenic load, and many other factors, including anthropogenic and technologic influences [13]. Arctic estuaries provide essential habitat for migratory birds, fish and marine mammals [12].

Approximately 1000 km^3 of freshwater flows through the estuaries of the Ob and the Yenisei rivers annually. With the runoff of these rivers an enormous amount of allochthonous substances (~$150 \cdot 10^6$ t/year) enters the estuarine zones. The composition of these substances reflects the entire spectrum of natural processes and economic activities in the watershed area. The degree of transformation of freshwater entering the Ob and Yenisei estuaries is determined by geomorphology features, level of water exchange, volume of river runoff and its seasonal dynamics [11, 14-17]. These estuaries should be given a very special place in the overall monitoring system of coastal areas. The anthropogenic and technologic impacts associated with mining, processing and transportation of minerals, and increasing exploitation of the Northern Sea Route are extremely strong here [18, 19].

The traditional method of monitoring river mouths and, in particular, estuaries is contact studies based on a system of stationary observations: a network of posts, control sections, stations, transects, etc., as well as various expeditionary works. Hydrological characteristics are calculated and predicted from the analysis of water samples obtained by grab samplers or hydrological probes. There are a number of methods used: empirical, hydrological, balance, etc. [5, 10, 11, 16, 20].

Over the past 40 years, remote sensing techniques have been increasingly used to monitor the state of coastal areas, rivers and their mouths. For this purpose, optical, multispectral, radar, and infrared airborne and satellite sensors of low, medium, high, and very high resolution are used [10, 21-25].

Visible and near-infrared data are generally used to track and assess changes in coastlines [21, 26-30], large river streamways [31] and winter freezing over the long reaches of large northern rivers [32]. The infrared range is used to determine surface temperature and thermal anomalies in coastal and estuarine areas [23, 31, 33]. Radar and synthetic-aperture radar (SAR) data provide key information for mapping coasts, flooding and inundation, wetland characterization, assessing soil subsidence along streams, analysis of surface changes in permafrost zones, etc. [21, 34-38]. River flow and related hydrodynamic processes, as well as estuarine and coastal water quality are assessed from remote sensing data of visible and near-infrared bands. It follows from the literature [39-46], that using data from these bands, one can estimate river flow level and map spatial distribution of suspended solids, turbidity, temperature and salinity in estuaries. Combining multispectral and SAR data and using machine learning methods enable mapping large rivers over vast areas [47].

Given the fact that most of the time the Arctic territory is inaccessible for the visible and near-infrared ranges (due to polar night or solid cloud cover), the microwave data, which are independent of solar illumination and cloud cover, become promising for the study of river estuaries [48]. First of all, these are satellite radar data and, second, satellite microwave radiometry data.

Akimov et al. [49] present the results of a study of the zone of fresh and salt waters mixing (the transition zone) in the estuaries of the Ob and the Yenisei in the Kara Sea using SAR ERS-1/2 satellite data. Satellite data were compared with contact measurements obtained during Kara Sea expeditions (KAREX). The expeditions were conducted in 1994 and 1995 by the Arctic and Antarctic Research Institute (AARI). Transition zones were detected in 70 images out of 89. However, the study left open many questions, in particular concerning the differences in the spatial distribution of the transition zones derived from satellite data and contact measurements. Studies of winter hydrology and ice regime of the Ob and Yenisei estuaries based on SAR data (ERS, RADARSAT, Envisat) are discussed by Melentyev et al. [50, 51]. Melentyev et al. [51] compare SAR data with the results of synchronous monitoring campaigns onboard icebreaker "Kapitan Dranitsyn" (April – May 1998) and nuclear icebreakers "Vaygach" and "Taymyr" (1993) as well as the data of multispectral "Resours-O1" satellite instrument. In Melentyev et al. [50], SAR data are analyzed together with climate characteristics. These studies highlight the prospects of radar imaging in assessing spatial and temporal variability of ice cover, detecting different types of ice, determining the beginning of ice formation and ice breakup, identifying polynyas, etc.

The use of satellite microwave radiometry in the study of river basins and estuaries began only in the XXI century. This happened so late because spatial resolution of the data is rather low (several kilometers and more). However, the possibility of obtaining information from vast areas, high frequency of observation in high latitudes, independence of the data of solar illumination and atmospheric conditions, sensitivity to subsurface processes, and low power consumption make satellite microwave radiometry a promising tool for monitoring the Earth surface [52]. Satellite microwave radiometry data are currently being used to determine flooding and underflooding in the vicinity of a river channel [53] and to estimate flooding extension on a global scale [54]. A pioneering study on flood area estimation is the work of Stippel et al. [55] presenting the results of Amazon basin flooding derived from SMMR (Scanning Multichannel Microwave Radiometer) data. The degree of flooding is obtained using the linear mixing model of microwave signatures from the underlying landscape (soil, vegetation) and the water surface. The brightness temperatures of these surfaces are very different. Subsequently, this method of monitoring flooded areas was improved using data from more modern AMSR-E (Advanced Microwave Scanning Radiometer for EOS) and SSM/I (Special Sensor Microwave/Imager) satellite radiometers with higher spatial resolution [53, 56-58]. Umbert et al. [59] presented a study of the salinity of the upper desalinated water layer of the Kara Sea and the Laptev Sea obtained from SMOS data. The results showed that the surface layer salinity is in a negative linear correlation with the concentration of detrital matter carried out by the Ob, Yenisei, and Lena rivers.

Tikhonov et al. [60, 61] discuss the results of a study of phenological phases of five large freshwater lakes (Baikal, Ladoga, Guron, Great Bear, and Great Slave) using data from MIRAS (Microwave Imaging Radiometer using Aperture Synthesis) of the SMOS satellite. In the study, multiyear seasonal

variations of brightness temperature in the central parts of the lakes are analyzed and compared with theoretical model calculations. This has allowed identifying three distinct time regions of brightness temperature values for freezing freshwater lakes. The first time region (TR1) with lowest brightness temperature corresponds to the radiation from ice-free water surface. The second time region (TR2) features rise and sustained stabilization of brightness temperature at an intermediate level and corresponds to the radiation from stable ice cover on the lake surface. The third time region (TR3) marks maximal brightness temperature as a result of a short-term (~ 20–50 days) sharp increase by 40–90 K and corresponds to the period of a drastic change in ice cover structure (intense destruction and melt). The work is continued by Tikhonov et al. [62] with the study of seasonal brightness temperature dynamics derived from SMOS data at three sites in the Gulf of Ob. Comparison of the satellite data with model results shows that in the freshwater part of the gulf (southern and central regions), the dynamics of brightness temperature is similar to lakes. However, in its "marine" part (northern region), there is no such similarity as no distinct TR2 can be observed on the brightness temperature curve. With the onset of freeze-up, brightness temperature strongly increases from the open water values (TR1) directly to the TR3 values which in this case correspond to stable ice cover. Then it remains relatively stable up to the beginning of ice cover destruction. The authors explain such change in the brightness temperature dynamics in the marine part of the gulf by an increase in salinity of water under the ice cover. The appearance of brackish water under ice leads to an increase in radiation absorption in the lower ice layer which is in contact with the water surface. This in turn leads to an increase in the brightness temperature which becomes comparable with that of decaying freshwater ice. The obtained results open the way to determining the transition zone in large estuaries of the Russian Arctic during the freezing period using satellite microwave radiometry data.

This article presents the results of a theoretical study of 2012–2018 seasonal and interannual variations of microwave radiation in different areas of the Gulf of Ob during the freezing period using SMOS MIRAS data. The study was carried out for the entire water area of the gulf (13 sites) and for one site located far from the estuary in the Kara Sea. Theoretical modeling of ice cover microwave radiation was carried out together with an analysis of the river runoff to the gulf, changes in climate characteristics of the Ob River watershed and territories adjacent to the gulf. The shift of the transition zone during the freezing period depending on river runoff to the Gulf of Ob and interannual climate changes in the adjoining territories of the watershed was examined.

STUDY AREA

The Gulf of Ob is the largest gulf of the Kara Sea (Fig. 1, left). It is located between the Gydansky and Yamal peninsulas (Fig. 1, left). Its length is about 800 km, width is 30-90 km, maximum depth does not exceed 28–30 m, and average depth is 10–15 m. The total area of the gulf is 40800 km^2, and its water volume is 400 km^3. In the south, during high water it resembles a river, and during low water a reservoir or lake. In the Gulf of Ob, two primary water masses, river and sea, come into contact forming a transition zone. The transition zone is a migrating phenomenon and during open water can be found between 71°N and 72°N (Fig. 1, right). Thus, two large areas with moving boundaries can be distinguished in the Gulf of Ob: the freshwater part and the marine part. The latter is bounded from the south by a salinity (mineralization) isohaline of 0.5‰ [16, 63, 64].

The Gulf of Ob lies almost entirely within the tundra zone. Average duration of the freezing period varies from 250 to 300 days. The hydrological regime during open water depends on a large number of factors. During high water, the determining factor is the river flow. During low water, the effect of meteorological factors, especially wind and associated storm surges, the amplitude of which can reach 3-4 m, increases sharply [63, 64].

As the major tributary to the Gulf of Ob with 75–76% of its total inflow, the Ob River has a determining significance for the hydrological regime of the Gulf of Ob and the processes occurring in it. Several other rivers flow into the Gulf of Ob: rivers Nadym and Nyda in the southeast, the Taz River opening to the Taz Gulf in the east and a number of smaller rivers from the Yamal Peninsula in the west.

The basin of the Ob is one of the largest in Siberia, its area reaches 2770000 km^2. From south to north, the river crosses a number of natural and climate zones from the Altai Mountains through semi-desert, steppe, forest-steppe, taiga to tundra. A significant part of the river feeding is snow (~55%), 25% is rainfall, and 20% is groundwater [63]. A distinctive feature of the Ob River is its giant watershed, much of which (~75%) is heavily marshy. Over most of its length (55%) the river flows through permafrost-free territory. In its lower reaches, the Ob flows in the zone of discontinuous and island permafrost, and only the river mouth and its estuary are located in the permafrost zone [65]. The Ob belongs to rivers with a prolonged spring-summer flood. Beginning in October and continuing throughout the winter, the river is mainly fed by groundwater, and its runoff sharply decreases at this time [54, 66].

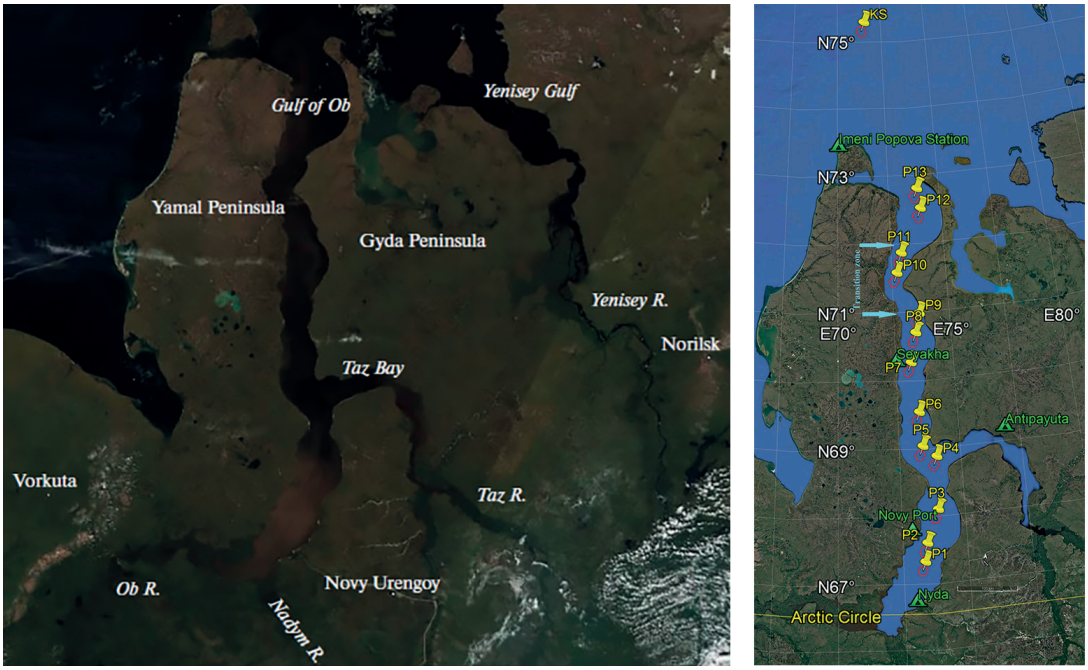

Fig. 1. Study area (the Gulf of Ob and the Kara Sea). Left: Terra MODIS image of 05.07.2016. Right: map of the area where yellow numbered pins are selected study sites with their numbers; red polygons are SMOS L1C cells corresponding to each selected study site; green triangles show weather stations; blue arrows show the location of the transition zone during open water

Рис. 1. Район исследования (Обская губа и Карское море). Слева: снимок Terra MODIS от 05.07.2016. Справа: карта района, где желтые пронумерованные значки - выбранные участки исследования с указанием их номеров; красные многоугольники - ячейки SMOS L1C, соответствующие каждому выбранному участку исследования; зеленые треугольники - метеостанции; синие стрелки показывают расположение фронтальной зоны в период открытой воды

DATA DESCRIPTION

Satellite data

Thirteen study sites (P1–P13) were selected across the entire water area of the Gulf of Ob plus one site located in the central part of the Kara Sea (see Fig. 1, right). For all selected sites, SMOS MIRAS data were obtained for the period from 2012 to 2018. Specifically, the SMOS L1C product version v620 was used [67]. The L1C product data are mapped to a discrete hexagonal DGG ISEA 4H9 geodetic grid [68]. The grid cells corresponding to each selected site are shown in Fig. 1, and the coordinates of their centers are listed in Table 1. The linear size of the cell is 15 km. The L1C product is built from the SMOS MIRAS data with a wavelength of 21 cm (frequency 1.4 GHz) and a resolution of 35×65 km for vertical (V) and horizontal (H) polarizations at a viewing angle of 42.5°. A continuous data archive for the period from 2012 to the present is stored on the servers of the European Space Agency (ESA).

Table 1

Center coordinates of the analyzed SMOS L1C cells.
DGG ID (Discrete Global Grid ID) is SMOS cell identification number

Таблица 1

Координаты центров анализируемых ячеек SMOS L1C.
DGG ID (Discrete Global Grid ID) - идентификационный номер ячейки SMOS

Site	DGG ID	Latitude, °N	Longitude, °E
P1	4050014	67.21	73.22
P2	4051040	67.49	73.33
P3	4053091	67.98	73.82
P4	4055657	68.76	73.88
P5	4055659	68.92	73.34
P6	4057199	69.42	73.27
P7	4059253	70.15	73.03
P8	4060792	70.58	73.30
P9	4061818	70.86	73.50
P10	4062848	71.46	72.59
P11	4063874	71.75	72.83
P12	4066949	72.39	73.87
P13	4067975	72.68	73.75
Kara Sea (KS)	4075674	75.18	71.38

Climate data

Climate data for the study area were obtained from meteorological stations (M), marine hydrometeorological stations (MH), and hydrological stations (HS) (http://www.sevmeteo.ru/company/stations.php, accessed June 10, 2022), and from the weather web archive (https://rp5.ru, accessed June 10, 2022). Fig. 1 on the right shows the locations of Nyda M, Imeni Popova MH, Novy Port MH, Antipayuta M and Seyakha HS. Table 2 shows their coordinates.

Table 2

Stations in the area of the Gulf of Ob

Таблица 2

Метеостанции в районе Обской губы

Weather station	Latitude, °N	Longitude, °E	Height, m
Nyda N	66.62	72.95	10
Novy Port MH	67.68	72.87	12
Antipayuta M	69.10	76.87	3
Seyakha HS	70.17	72.52	16
Imeni Popova St. MH	73.33	70.05	6

Table 3

Stations on the Ob River

Таблица 3

Станции и посты на реке Обь

Ob River sections	Locality, Region	Latitude, °N	Longitude, °E
Upper Ob	Barnaul, Altai Krai, Russia	53.35	83.78
Upper Ob	Ordynskoye, Novosibirsk Oblast, Russia	54.37	81.90
Upper Ob	Molchanovo, Tomsk Oblast, Russia	57.58	83.77
Middle Ob	Kolpashevo, Tomsk Oblast, Russia	58.31	82.90
Middle Ob	Kargasok, Tomsk Oblast, Russia	59.06	80.86
Middle Ob	Nizhnevartovsk, Khanty-Mansi Autonomous Okrug, Russia	60.94	76.56
Lower Ob	Sytomino, Khanty-Mansi Autonomous Okrug, Russia	61.30	71.29
Lower Ob	Oktyabrskoye, Khanty-Mansi Autonomous Okrug, Russia	62.46	66.04
Lower Ob	Salekhard, Yamalo-Nenets Autonomous Okrug, Russia	66.53	66.61

The Ob River with the Katun River, one of main Ob tributaries, cross the entire territory of Russia from south to north, flowing through a number of natural and climate zones. By the nature of the river network, feeding conditions and flow formation, the Ob is divided into 3 sections: Upper Ob (from the confluence of Biya and Katun rivers to the mouth of the Tom River), Middle Ob (up to the mouth of the Irtysh River) and Lower Ob (up to the Gulf of Ob). To analyze the climate conditions along the Ob River in the study period (2012–2018), data from several weather stations in different parts of the river were obtained from the weather web archive (https://rp5.ru, accessed June 10, 2022). The locations of the weather stations are listed in Table 3.

Glaciological data

The characteristics of ice (thickness) and snow cover (height and density) in the Gulf of Ob were obtained for the period 2010–2017 at Novy Port MH. They were measured by A.I. Sinitsky, one of the authors of this article, and Yu.I. Prilepsky, Head of Novy Port MH of the Northern Agency for Hydrometeorology and Environmental Monitoring (http://www.sevmeteo.ru/company/stations.php, accessed June 10, 2022). The data were averaged and approximated by smooth curves shown in Fig. 2. In the other parts of the Gulf of Ob, ice and snow characteristics differ little from those obtained at New Port MH [69].

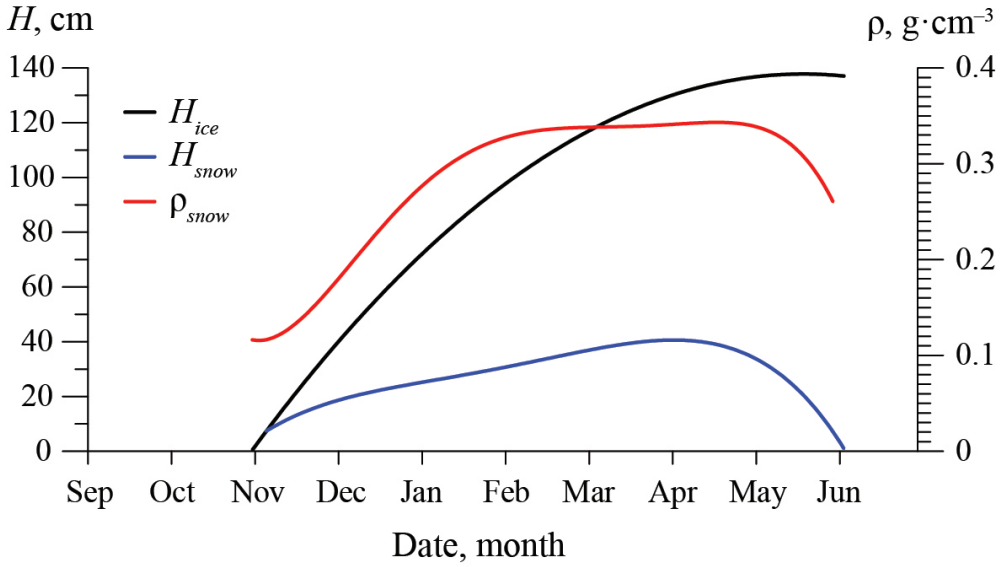

Fig. 2. Eight-year averages (2010–2017) of seasonal variations in ice thickness (H_{ice}), snow depth (H_{snow}) and snow density (ρ) in the Novy Port MH area of the Gulf of Ob

Рис. 2. Усреднённые за 8 лет (2010–2017) сезонные зависимости толщины льда (H_{ice}), высоты снежного покрова (H_{snow}) и плотности снега (ρ) в Обской губе в районе МН Новый порт

Hydrological data

Data on hydrological characteristics of the Gulf of Ob (temperature, water salinity, temperature and salinity profile by depth) were obtained from works of [16, 20, 63, 64]. They give water temperature and salinity at water surface and beneath in the summer and autumn seasons. There are almost no data on contact measurements of water salinity in the freezing period, neither at the surface nor at depth. Voynov et al. [64] show the results of winter salinity measurements under landfast ice that were made mainly from 1966 to 1988, i.e., 30–55 years ago. As noted in the work, the measurements were carried out irregularly and were of rather poor quality, not allowing a statistical analysis. Allegedly, as cited by Lapin [63], the farthest penetration of seawater into the Gulf of Ob, as far as the Taz Gulf (69°03' N), was observed at the end of the freezing period, however, no reliable documentary confirmation is available.

Since most of the runoff to the Gulf of Ob is supplied by the Ob River (>75%), an analysis of interannual river runoff near the city of Salekhard was undertaken. Salekhard is located 287 km from the mouth of the Ob. Runoff data for 2011–2018 were obtained from the following servers: ArcticGRO (https://arcticgreatrivers.org/data/, accessed June 10, 2022), ArcticRIMS (https://rims.unh.edu//data.shtml, accessed June 10, 2022) and R-ArcticNet (https://www.r-arcticnet.sr.unh.edu/v4.0/index.html, accessed June 10, 2022).

They are presented in Fig. 3 which shows a drastic change, depending on the year, in the river runoff in the warm half of the year (May – October). In the cold half of the year (November – April), the fluctuations of the river flow are not so significant. Bulavina [66] shows that the runoff of the Ob River is determined by the water content of the warm half-year. The runoff of the warm half-year is mostly influenced by the amount of solid precipitation of the preceding cold half-year and the precipitation of the warm half-year. The most significant is the amount of solid precipitation in the Upper and Middle Ob basins [66].

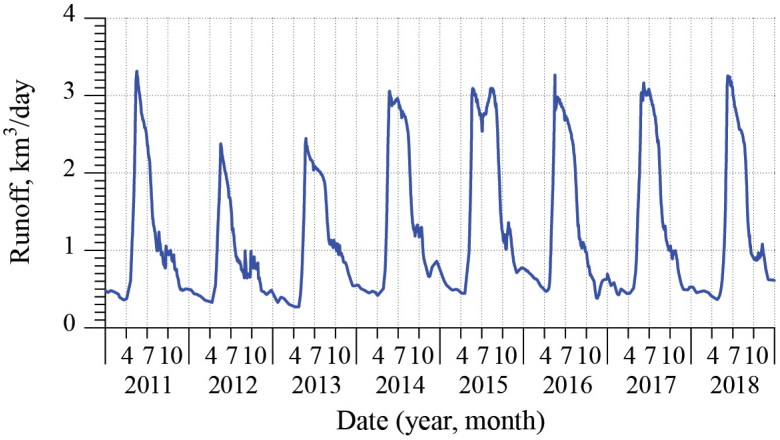

Fig. 3. Runoff of the Ob River near Salekhard for the period 2011–2018

Рис. 3. Сток реки Обь у города Салехард за период 2012–2018 гг.

MODEL

To interpret and analyze the seasonal variations in the brightness temperature of the Gulf of Ob regions during the freezing period, we used the radiation model of layered inhomogeneous non-isothermal medium [52]. The model was adapted for the case of the "fresh/sea water – ice cover (two layers) – snow cover – atmosphere" radiating system. A detailed description of the model for both marine and freshwater areas is given by Tikhonov et al. [61, 70]. In our case, the radiating system is an environment consisting of several layers: a fresh/sea water surface, above it a thin layer of wet ice (due to contact with the water), next is a layer of ice (wet or dry, depending on temperature conditions), above it a snow cover and then a thick layer of atmosphere (Fig. 4). As was shown by Demir et al. [71], such configuration enables a good model description of microwave radiation of an ice cover. Depending on the hydrological regime of the modeled region of the Gulf of Ob, the ice cover may be either freshwater or seawater.

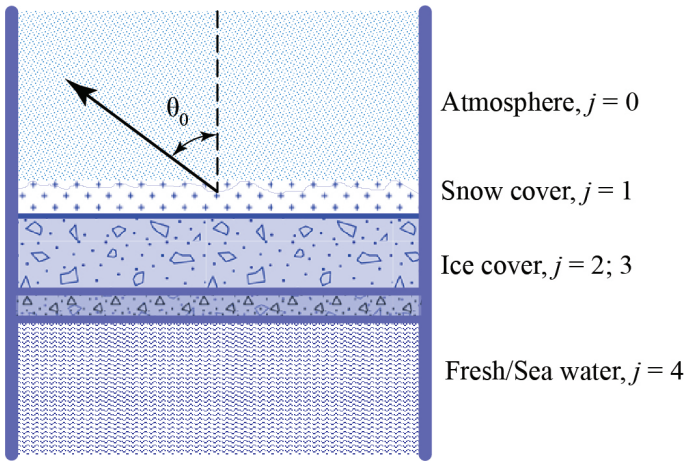

Fig. 4. Model of the "fresh/sea water – wet ice cover – ice cover – snow cover – atmosphere" radiative system

Рис. 4. Модельное представление излучающей системы «пресная/морская вода – влажный ледяной покров – ледяной покров – снежный покров – атмосфера»

Brightness temperature TBr of such a system is determined from the expressions discussed in detail by Sharkov [52] and Tikhonov et al. [61, 70]:

$$T_{Br}^{v} = \sum_{j=1}^{3} \frac{T_j \left|W_j\right|^2}{\left|1 - r_j^- r_j^+ \exp(2i\psi_j)\right|^2} \left[\begin{array}{c} \left(1 - \exp(-2\,\mathrm{Im}\,\psi_j)\right) \cdot \left(1 + \left|r_j^- \exp(i\psi_j)\right|^2\right) + \\ +4 \dfrac{\mathrm{Im}\,\psi_j}{\mathrm{Re}\,\psi_j} \mathrm{Re}\left(r_j^- \exp(i\psi_j)\right) \cdot \mathrm{Im}\left(\exp(i\psi_j)\right) \cdot \left(\dfrac{\left|k_{z_j}\right|^2 - k_x^2}{\left|k_j\right|^2} \right) \end{array} \right] \times$$

$$\times \frac{\mathrm{Re}\,Z_j}{\mathrm{Re}\,Z_0} + T_4 \left|W_4\right|^2 \frac{\mathrm{Re}\,Z_4}{\mathrm{Re}\,Z_0}, \qquad (1)$$

$$T_{Br}^{h} = \sum_{j=1}^{3} \frac{T_j \left|W_j\right|^2}{\left|1 - r_j^- r_j^+ \exp(2i\psi_j)\right|^2} \left[\begin{array}{c} \left(1 - \exp(-2\,\mathrm{Im}\,\psi_j)\right) \cdot \left(1 + \left|r_j^- \exp(i\psi_j)\right|^2\right) + \\ +4 \dfrac{\mathrm{Im}\,\psi_j}{\mathrm{Re}\,\psi_j} \mathrm{Re}\left(r_j^- \exp(i\psi_j)\right) \cdot \mathrm{Im}\left(\exp(i\psi_j)\right) \end{array} \right] \times$$

$$\times \frac{\mathrm{Re}\,Z_j}{\mathrm{Re}\,Z_0} + T_4 \left|W_4\right|^2 \frac{\mathrm{Re}\,Z_4}{\mathrm{Re}\,Z_0},$$

where the upper index of T_{Br} denotes:
v — vertical polarization;
h — horizontal polarization;
index *j* denotes layer of the medium;
the underlying layer ($j = 4$) has semi-infinite thickness;
k_j is wave vector in layer *j*;
T_j is temperature of layer *j*;
r_j^+, r_j^- are reflection coefficients from the upper and lower boundaries of layer *j*, respectively;
Ψ_j is wave phase overrun across layer *j*;
W_j is transmission coefficient from the inner side of the upper boundary of layer *j* to the snow-atmosphere boundary;
Z_j is wave impedance of layer *j*.
The characteristics of each layer are found from the following expressions:

$$W_j = \prod_{m=1}^{j} \frac{Z_{m-1}^{in+} + Z_{m-1}}{Z_{m-1}^{in+} + Z_m} \exp\left(i\psi_{m-1}\right), \qquad Z_j^{in+} = Z_j \frac{Z_{j-1}^{in+} - iZ_j \,\mathrm{tg}\,\psi_j}{Z_j - iZ_{j-1}^{in+} \,\mathrm{tg}\,\psi_j}, \qquad Z_j^{in-} = Z_j \frac{Z_{j+1}^{in-} - iZ_j \,\mathrm{tg}\,\psi_j}{Z_j - iZ_{j+1}^{in-} \,\mathrm{tg}\,\psi_j},$$

$$\psi_j = k_{z_j} h_j, \qquad k_{z_j} = k_j \cos\theta_j, \qquad k_x = k_0 \sin\theta_0, \qquad k_j = \frac{2\pi\sqrt{\varepsilon_j}}{\lambda}, \qquad \cos\theta_j = \sqrt{\frac{\varepsilon_j - \varepsilon_0 \sin^2\theta_0}{\varepsilon_j}},$$

$$r_j^+ = \frac{Z_{j-1}^{in+} - Z_j}{Z_{j-1}^{in+} + Z_j}, \quad r_j^- = \frac{Z_{j+1}^{in-} - Z_j}{Z_{j+1}^{in-} + Z_j}, \quad Z_j = \begin{cases} \dfrac{1}{\sqrt{\varepsilon_j}\cos\theta_j} & -\text{horizontal polarization}, \\ \dfrac{\cos\theta_j}{\sqrt{\varepsilon_j}} & -\text{vertical polarization}, \end{cases} \qquad (2)$$

where Z^{in+}_j is input impedance in layer *j* at the lower boundary for a wave propagating upward;
Z^{in-}_j is input impedance in layer *j* at the upper boundary for a wave propagating downward;
h_j is thickness of layer *j*;
λ is radiation wavelength;
θ_0 is viewing angle (see Fig. 4);
ε_j is complex dielectric constant of layer *j*.

Thus, the radiation of the system is determined by the physical temperature and the complex dielectric constant of each layer. The layer (ice and snow) complex dielectric constant was determined using the quasi-wave model of effective dielectric constant of a dispersed medium [61, 70, 72]. As the model input parameters (air, snow, and ice temperatures; snow density; ice cover salinity; average size of snow ice grains, air pores, brine and water inclusions in ice; their size dispersions, etc.) data were obtained from M, MH, and HS closest to the study site (see Fig. 1 and Table 2). Also, the average parameters of snow, freshwater, and sea ice typical of the Arctic region were taken from the literature [73-79].

During open water, brightness temperature of selected sites was determined as the product of water surface emissivity and thermodynamic temperature [80].

RESULTS AND DISCUSSION

Satellite data and modeling

In order to analyze brightness temperature dynamics in different study sites of the Gulf of Ob during the freezing period, model calculations were performed. The results were compared with satellite data.

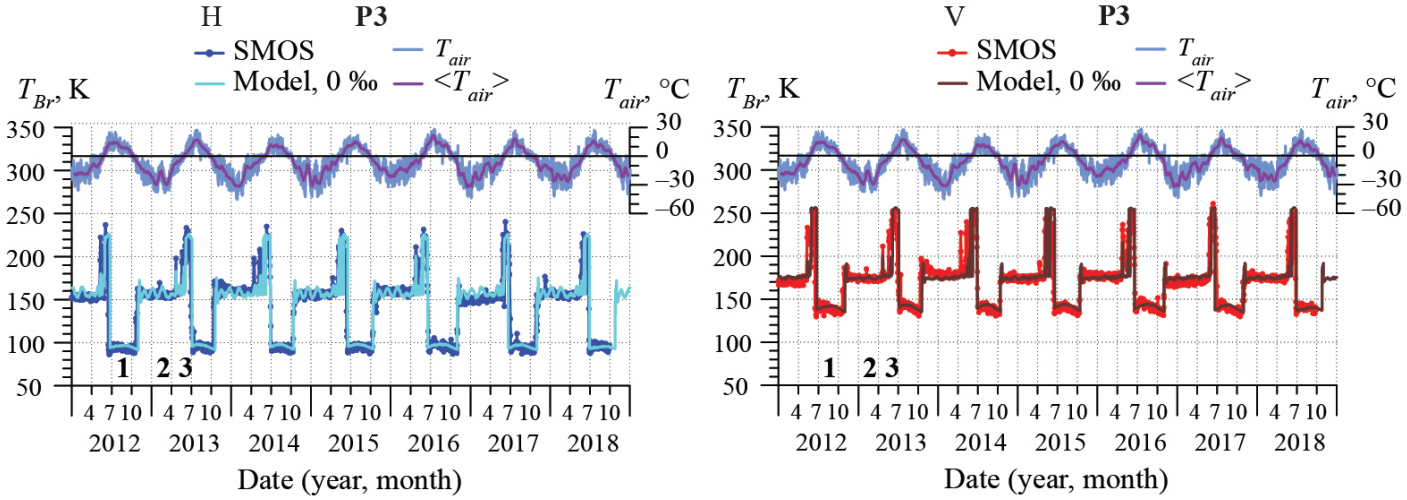

Fig. 5. Seasonal dynamics of brightness temperature at Site P3 in the Gulf of Ob from SMOS data at H (left panel, lower graph) and V (right panel, lower graph) polarizations. The upper graphs of each panel show daily and 2-week average air temperature. Blue and red lines and symbols are the SMOS data; cyan and dark brown lines are the modeling results for a salinity of 0 ‰. Numbers below the brightness temperature lines indicate the three time regions of brightness temperature values: 1 — open water (TR1), 2 — ice cover (TR2), 3 — ice destruction (TR3)

Рис. 5. Сезонная динамика яркостной температуры на площадке P3 в Обской губе по данным SMOS при H (левый рисунок, нижний график) и V (правый рисунок, нижний график) поляризациях. Верхние графики каждого рисунка показывают дневную и 2-недельную среднюю температуру воздуха. Синие и красные линии и символы - данные SMOS; голубые и темно-коричневые линии - результаты моделирования для солености 0 ‰. Цифры под линиями яркостной температуры указывают на три временные области значений яркостной температуры: 1 - открытая вода (TR1), 2 - ледяной покров (TR2), 3 - разрушение льда (TR3)

Figure 5 shows the brightness temperature dynamics at Site P3 (see Fig. 1, right) derived from the MIRAS data as well as the theoretical dependencies calculated using formulas (1)–(2). It should be noted that at sites P1 and P2 the brightness temperature dynamics is identical to P3. Analysis of the graphs shows that they are very similar to the seasonal brightness temperature dynamics of freshwater lakes [60, 61]. Comparison of satellite data and

modeling revealed three time regions of brightness temperature values for freshwater lakes. The first region (TR1) is associated with radiation from ice-free water surface. The second (TR2) marks stable ice cover on the lake surface. The third time region (TR3), characterized by a short-term sharp increase in brightness temperature by several tens of K, corresponds to the period of intense destruction and melt of the ice cover. In Fig. 1, exactly the same time regions TR1-TR3 are present on the brightness temperature graphs for freshwater sites (P1–P3). Here, the correlation between air temperature and brightness temperature corresponding to the phenological phases of the Gulf of Ob is well traced (see Fig. 5). Ice freeze-up begins when the air temperature drops below zero degrees Celsius. After ice cover is established, the dynamics of brightness temperature is quite stable and corresponds to that of average air temperature. The destruction of the ice cover begins when air temperature stays at zero for some time and then becomes positive.

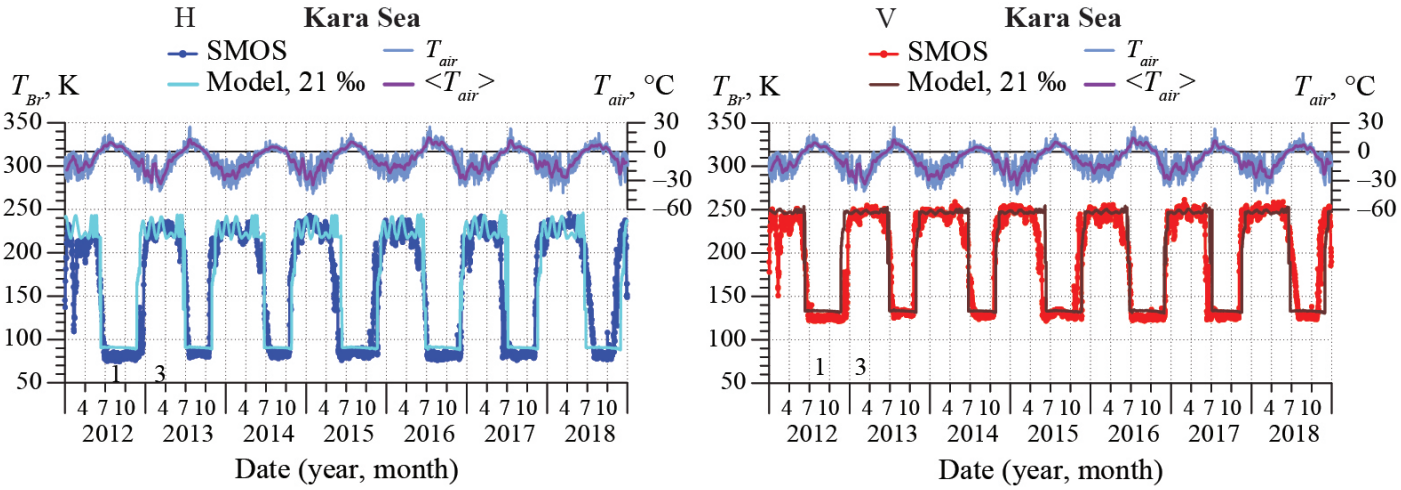

Fig. 6. Seasonal dynamics of brightness temperature in the Kara Sea from SMOS data. The notations are the same as in Fig. 5. Modeling is performed for a salinity of 21 ‰. Numbers below the brightness temperature lines show two time regions of brightness temperature: 1 — open water (TR1), 3 — stable ice cover and ice destruction (TR3)

Рис. 6. Сезонная динамика яркостной температуры в Карском море по данным SMOS. Обозначения те же, что и на рис. 5. Моделирование выполнено для солености воды 21 ‰. Цифры под линиями яркостной температуры показывают две временные области яркостной температуры: 1 - открытая вода (TR1), 3 - устойчивый ледяной покров и разрушение льда (TR3)

The site in the Kara Sea (Fig. 1, right), in comparison with the freshwater sites of the Gulf of Ob, demonstrates a different brightness temperature dynamics. The difference is determined by the absence of TR2 (Fig. 6). With ice freeze-up, brightness temperature leaps from open water values to values recorded in TR3 at freshwater sites (see Fig. 5), then it remains relatively stable up to the beginning of ice destruction. The leap of over 130 K occurs in the period when air temperature drops and remains below zero for some time. As a result, brightness temperature reaches the values corresponding to ice destruction in the freshwater sites (compare Figs. 5 and 6). But in the Kara Sea, such values correspond to the ice cover period. During this period, for a long time (5–7 months), brightness temperature is not as stable as in TR2 at freshwater sites, and varies in the counter-phase with the dynamics of average air temperature. Closer to the spring-summer season, when air temperature periodically exceeds 0°C, brightness temperature becomes even more unstable, which can be explained by snow and ice periodic melt/freeze processes. Ice destruction begins when average air temperature exceeds 0°C.

Calculations using formulas (1)–(2) showed that the change in the seasonal brightness temperature dynamics at the Kara Sea site is related to a change in water salinity. For the freshwater part of the Gulf of Ob (P1–P3), the calculation was performed for a water salinity of 0 ‰, whereas for the Kara Sea site salinity was assumed at 21‰, which corresponds to the real water salinity (20–25‰) in this part of the sea [81, 82]. An increase in salinity leads to a strong growth of the imaginary part of the dielectric constant of water near 1.4 GHz [52] that, in turn, leads to an increase in radiation absorption by wet ice. Schematically, the absorption and emission processes in ice and snow at sites P1-P3 and in the Kara Sea can be described as follows (Figs. 7, 8).

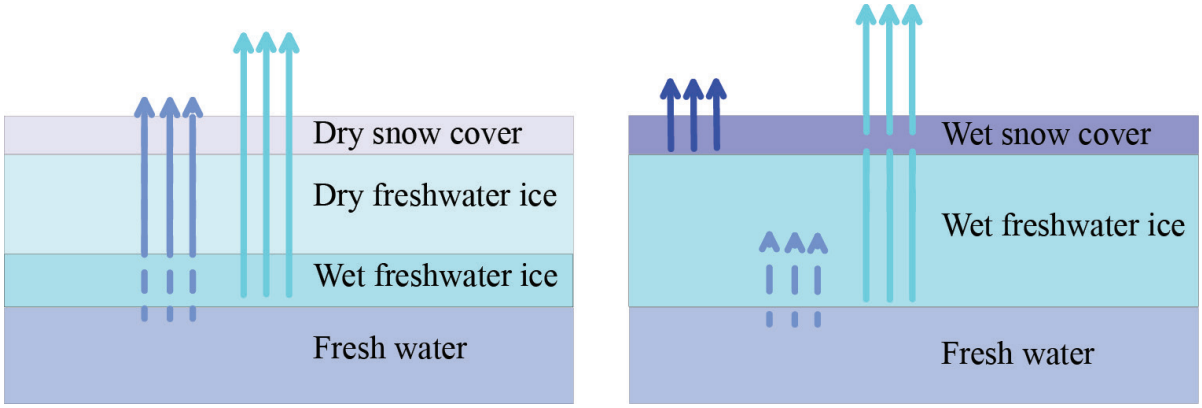

Fig. 7. Schematics of intrinsic microwave radiation of water, ice and snow for sites P1–P3 of the Gulf of Ob. Left: stable ice cover (TR2, see Fig. 5); Right: ice cover destruction (TR3, see Fig. 5)

Рис. 7. Схемы собственного микроволнового излучения воды, льда и снега для участков P1-P3 Обской губы. Слева: устойчивый ледяной покров (TR2, см. рис. 5); справа: разрушение ледяного покрова (TR3, см. рис. 5)

At Site P3, TR2 (see Fig. 5) is associated with stable ice cover. At the beginning, there is a strong increase in brightness temperature related to water freeze-up and appearance of a stable ice cover. Once established, the ice cover is characterized by brightness temperature determined by the seasonal course of average air temperature in this region. Dry snow and dry freshwater ice (without liquid water in its pores) have low dielectric losses at 1.4 GHz [80], 2014). Their radiation penetration depths in this range are much greater than the thickness of ice and snow cover in the Gulf of Ob [61, 62]. Consequently, dry freshwater ice and dry snow are transparent for this radiation range. In wet freshwater ice with inclusions of liquid water in its pores, the absorption of microwave radiation increases, and such ice starts emitting radiation. In TR2, the radiation pattern at sites P1–P3 can be represented as follows (see Fig. 7, left). Part of the radiation from the water surface is absorbed by the wet freshwater ice layer. However, such ice emits by itself and adds radiation to the water surface radiation. Dry snow cover and dry freshwater ice are transparent for the radiation from beneath.

TR3 at Site P3 (see Fig. 5) is characterized by a short-term sharp increase in brightness temperature by about 80 K. This is the period of intense ice cover destruction and ice and snow melt [61]. During this period, changes in the physical properties of the entire ice cover occur: cracks appear in large numbers and get saturated with water. The presence of liquid water in ice alters its dielectric properties causing a strong increase in absorption of microwave radiation [80]. Increased absorption leads to an increase in the brightness temperature of the ice cover. However, absorption sharply

decreases the penetration depth of freshwater ice [61, 62] turning it into a shield for the radiation rising from the water surface. The snow cover during this period has a thickness of several centimeters (see Fig. 2) and maximum wetness due to intense melt. At 1.4 GHz, the radiation penetration depth for such snow is small (10–20 cm), but greater than the thickness of the snow cover on ice [61, 62]. Therefore, the wet snow layer has the same effect on the ice cover radiation in TR3 as the wet ice layer in TR2 does on the water surface radiation (see Fig. 7, left). Only here the snow cover adds radiation to the radiation of melting ice. The resulting summary radiation characterizes TR3 for sites P1-P3 (Fig. 7, right). Thus, the seasonal brightness temperature dynamics of the freshwater part of the Gulf of Ob completely corresponds to that of freezing freshwater lakes [60, 61].

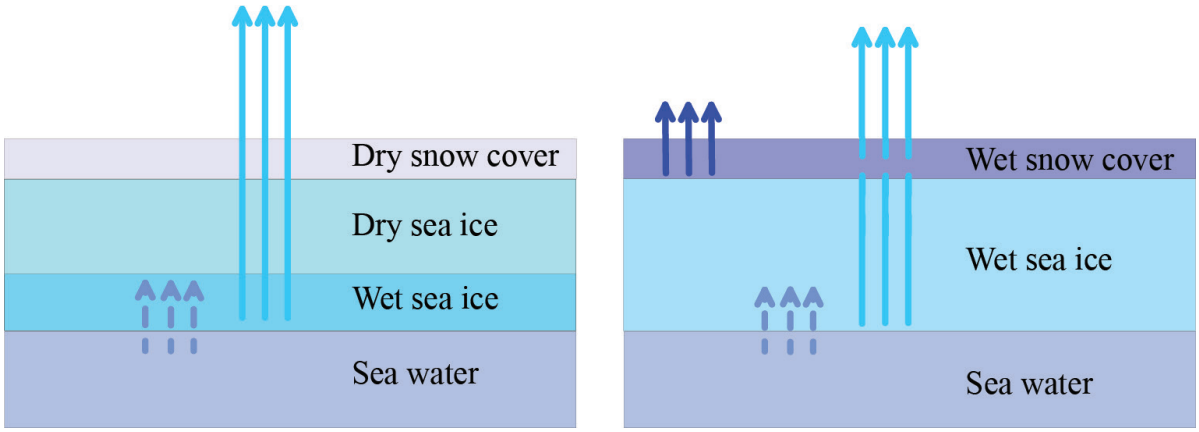

Fig. 8. Schematics of intrinsic microwave radiation of water, ice and snow at the Kara Sea site. Left: stable ice cover (beginning and middle of TR3, see Fig. 6); right: ice cover destruction (end of TR3, see Fig. 6)

Рис. 8. Схемы собственного микроволнового излучения воды, льда и снега на участке в Карском море. Слева: стабильный ледяной покров (начало и середина TR3, см. рис. 6); справа: разрушение ледяного покрова (конец TR3, см. рис. 6)

The peculiarity of the site in the Kara Sea is the absence of TR2 in the graph of interannual brightness temperature dynamics (see Fig. 6). Here, TR1 transforms directly into TR3 over a short period of time (about a month). Brightness temperature leaps by about 130–160 K depending on radiation polarization. The duration of TR3 for this site corresponds to the freezing period. Further, with the ice cover melt and decay TR3 changes over to TR1. At this site, ice is formed from salty water in contrast to P1–P3 of the Gulf of Ob where water remains fresh even in winter [16, 20, 63, 64]. This means much greater absorption of radiation in the lower ice layer that is in constant contact with salty water. The increased absorption in the lower ice layer, as compared to P1–P3, leads to an increase in the brightness temperature [83]. Due to the strong absorption, the lower (wet) ice layer shields the 1.4 GHz radiation from the water surface while its own radiation increases in comparison with freshwater ice (see Fig. 8, left). The conditions here are similar to the period of ice cover destruction at P1–P3 (see Fig. 7, right, and Fig. 8, left). At 1.4 GHz, the radiation from melting and decaying freshwater ice is practically similar in magnitude to the radiation from stable ice cover in the Kara Sea. Also, water salinity at the Kara Sea site explains a slightly delayed establishment of the ice cover there, as compared to P1–P3 (compare Figs. 5, 6).

The period of ice cover destruction and melt in the Kara Sea (end of TR3) differs slightly from the same period in the freshwater part of the Gulf of Ob (P1–P3). As ice begins to melt, many cracks and pores appear in it. They fill with

salt water from below and with fresh water from above. This further increases the absorption of radiation in the ice cover. The snow cover becomes wet and partly absorbs the radiation from the ice. At the same time, the wet snow itself starts emitting and adds its own radiation to that of the sea ice (see Fig. 8, right).

Microwave radiation modeling in the other selected sites of the Gulf of Ob obtained the following results.

Analysis of Site P4 showed that water salinity under the ice cover can vary 0–5‰ in different years (Fig. 9). In 2012, 2017 and 2018, winter water salinity was 0‰, and in 2014 and 2015 it was 5‰. In the other years considered, winter water salinity was between 0 and 5‰ (see Fig. 9). At Site P4, ice cover is formed from fresh water. However, in winter, for various reasons (they will be discussed below), the salinity of water under ice may increase. The lower ice layer (see Fig. 7, left) is then saturated with brackish water instead of fresh water. Consequently, absorption of radiation increases in this layer, but the layer itself emits more intense radiation. In this case, microwave radiation of Site P4, schematically, will appear intermediate between Fig. 7, left, and Fig. 8, left. The ice is freshwater, but its lower layer is saturated with brackish water. Brightness temperature varies depending on water salinity: both either increase or decrease. The seasonal and interannual dynamics of brightness temperature at Site P5 almost completely agree with those of P4.

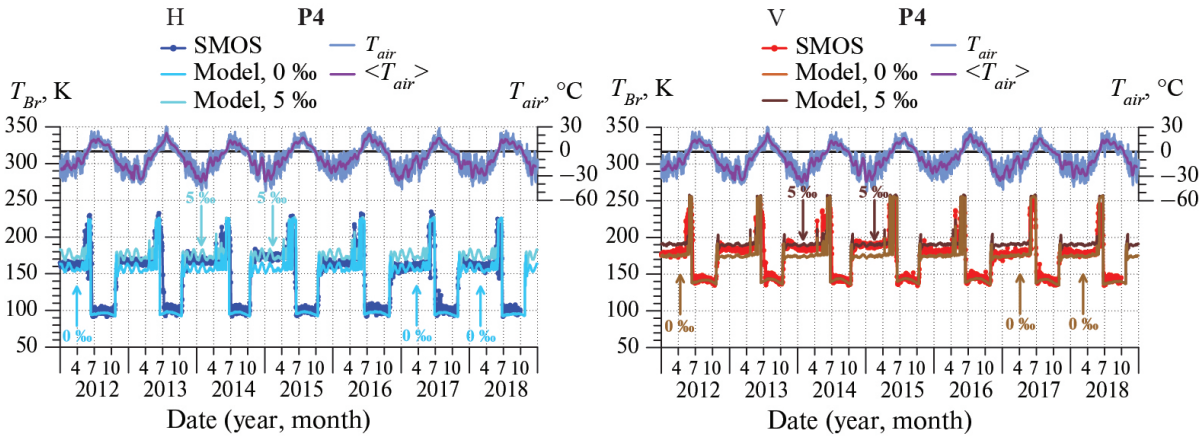

Fig. 9. Seasonal dynamics of brightness temperature at Site P4 from SMOS data. Notations are the same as in Fig. 5. Model results are sky blue and brown for a water salinity of 0‰ and cyan and dark brown for 5‰. Vertical arrows show fits of the satellite data to the model results at water salinity of 0 or 5‰

Рис. 9. Сезонная динамика яркостной температуры на участке P4 по данным SMOS. Обозначения те же, что и на рис. 5. Результаты моделирования представлены бирюзовым и коричневым цветом для солености воды 0 ‰ и голубым и темно-коричневым для 5‰. Вертикальные стрелки показывают соответствие спутниковых данных результатам моделирования при солености воды 0 или 5‰

At Site P6, model calculations agree with satellite data for under-ice water salinity at an average of 5‰ (Fig. 10). Here, as well as at P4, water salinity fluctuations in winter are noticeable across the years, though not so pronounced.

Analysis of Site P8 data showed that under-ice water salinity in winter in this part of the gulf is unstable and can vary greatly not only from year to year, but also during one winter season in the range from 5 to 15‰ (Fig. 11). Indeed, in 2014 and 2015, water salinity during the winter was 5‰, and in 2018, for most of the freezing period, it was 15‰. And in 2013 and 2016, under-ice water salinity varied from 5‰ at the beginning of winter to 15‰ at the end. At sites P7 and P9 (see Fig. 1, right), the seasonal and interannual brightness temperature dynamics are the same as at P8.

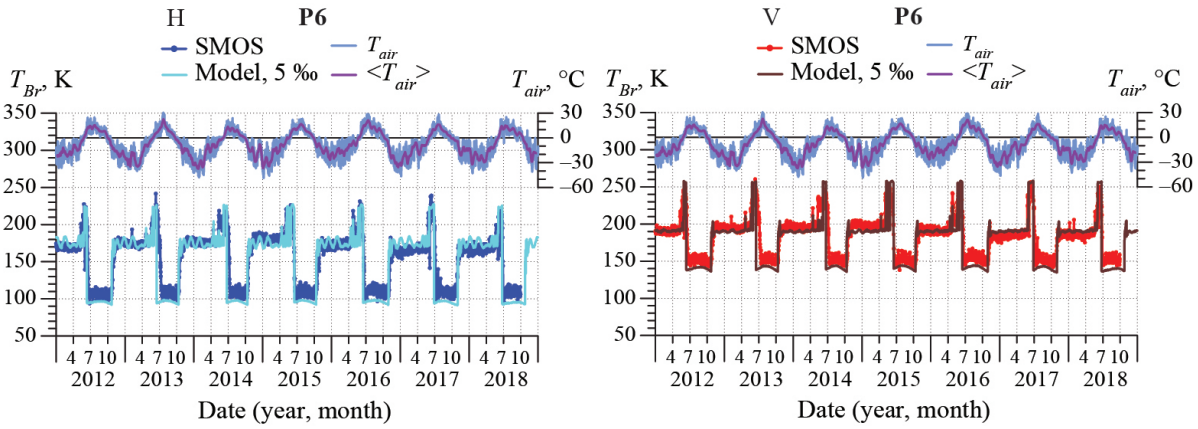

Fig. 10. Seasonal brightness temperature dynamics at Site P6 from SMOS data. The notations are the same as in Fig. 5. The modeling is performed for a water salinity of 5 ‰

Рис. 10. Сезонная динамика яркостной температуры на участке P6 по данным SMOS. Обозначения те же, что и на рис. 5. Моделирование выполнено для солености воды 5 ‰

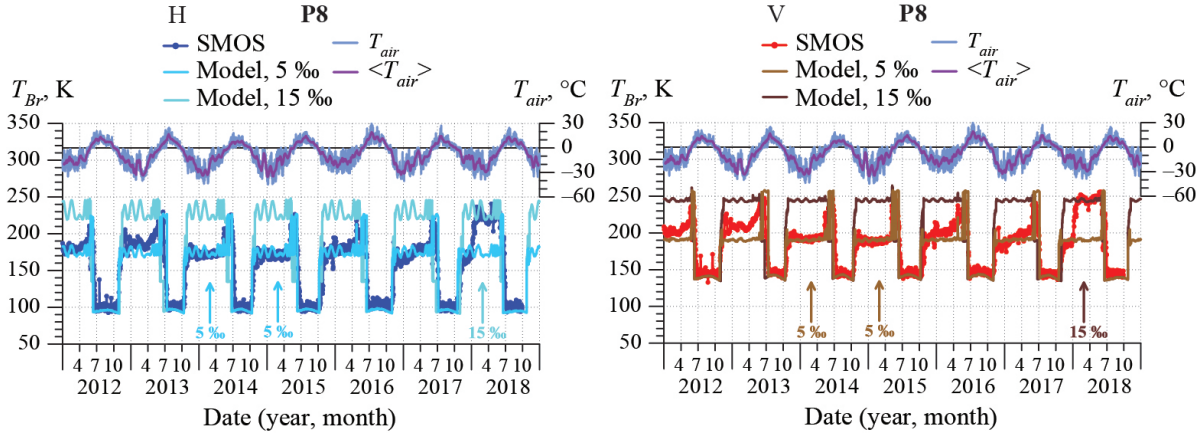

Fig. 11. Seasonal dynamics of brightness temperature at Site P8 from SMOS data. The notations are the same as in Fig. 5. Model results are sky blue and brown for a water salinity of 5‰ and cyan and dark brown for 15‰. Vertical arrows show fits of the satellite data to the model results at 5‰ or 15‰ water salinity

Рис. 11. Сезонная динамика яркостной температуры на участке P8 по данным SMOS. Обозначения те же, что и на рис. 5. Результаты моделирования выделены бирюзовым и коричневым для солености воды 5‰ и голубым и темно-коричневым для 15 ‰. Вертикальные стрелки показывают соответствие спутниковых данных результатам моделирования при солености воды 5 ‰ или 15 ‰

The seasonal and interannual brightness temperature dynamics at Site P10 are close to P8. However, the variation of under-ice water salinity from year to year is not as large and averages between 10 and 15‰ (see Fig. 12). The seasonal and interannual dynamics of brightness temperature at Site P11 almost completely mimic those at P10.

Analysis of sites P12 and P13 showed that in this part of the Gulf of Ob the seasonal and interannual brightness temperature dynamics do not differ from the Kara Sea site (compare Figs. 6 and 13). Here, ice is already formed from brackish water, as evidenced by numerous contact measurements made in autumn [16, 20, 63, 64] and irregular winter measurements (Fig. 14) [64, 84]. Figure 13 shows the model results at Site P13 for under-ice water salinity of 15‰.

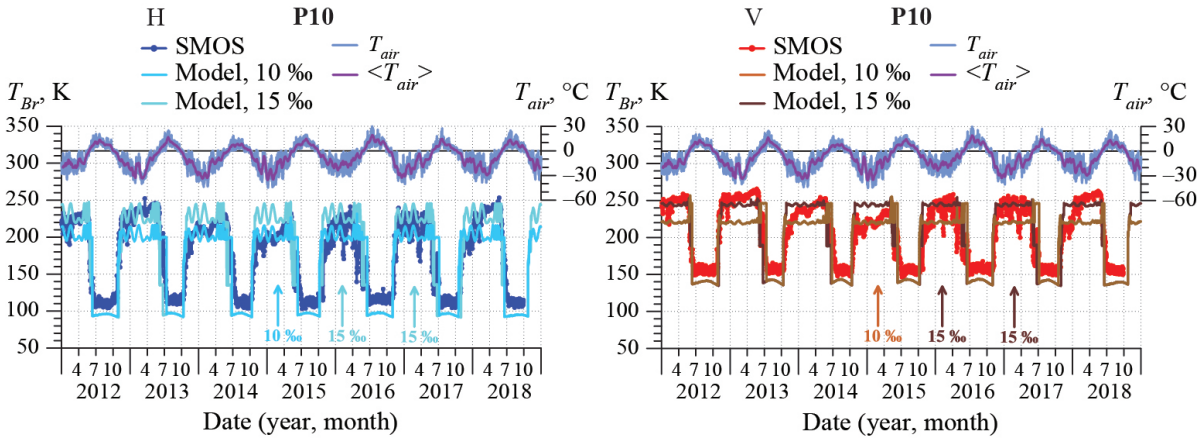

Fig. 12. Seasonal dynamics of brightness temperature at Site P10 from SMOS data. Notations are the same as in Fig. 5. Model calculations are sky blue and brown for a water salinity of 10 ‰ and cyan and dark brown for 15 ‰. Vertical arrows show fits of the satellite data to the model results at 10 or 15 ‰

Рис. 12. Сезонная динамика яркостной температуры на участке P10 по данным SMOS. Обозначения те же, что и на рис. 5. Модельные расчеты выделены бирюзовым и коричневым цветом для солености воды 10 ‰ и голубым и темно-коричневым для 15 ‰. Вертикальные стрелки показывают соответствие спутниковых данных результатам моделирования при 10 или 15 ‰

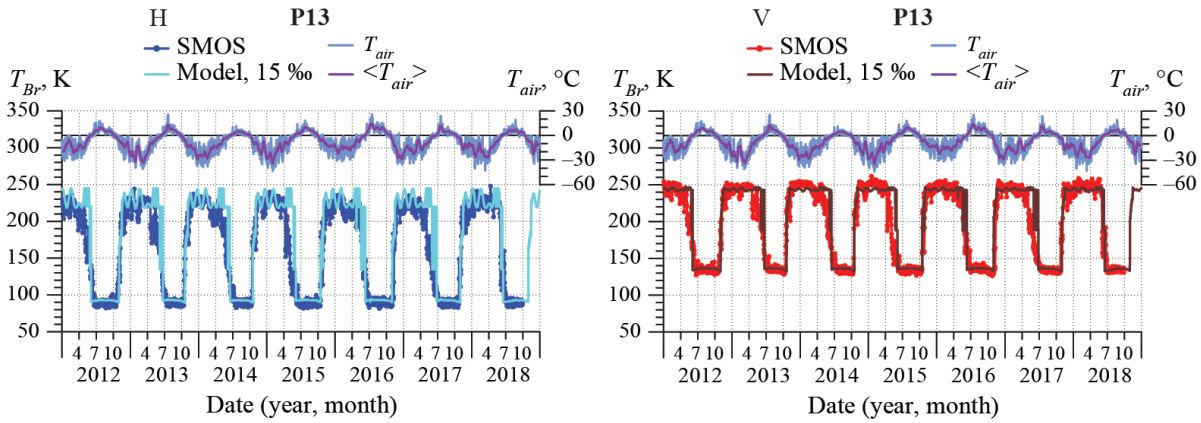

Fig. 13. Brightness temperature seasonal dynamics at Site P13 from SMOS data. The notations are the same as in Fig. 5. Modeling is performed for a water salinity of 15 ‰

Рис. 13. Сезонная динамика яркостной температуры на участке P13 по данным SMOS. Обозначения те же, что и на рис. 5. Моделирование выполнено для солености воды 15 ‰

Note that at P13, the winter water salinity reported by Voynov et al. [64] is 15‰, the same as used in the modeling for this site (compare Figs. 1 and 14 and Table 1). According to Voynov et al. [64], the winter water salinities at P8 and P10 are 3 and 9‰, respectively (compare Figs. 1 and 14 and Table 1). In the modeling for these sites, nearly the same values of water salinity (5 and 10‰, respectively) were used.

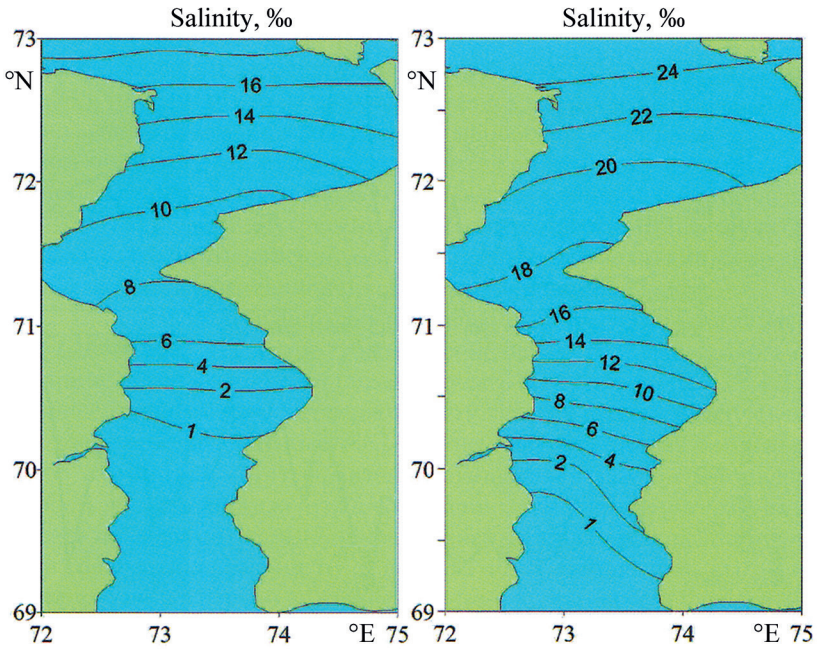

Fig. 14. Winter mean multiyear distribution of water salinity in the Gulf of Ob at the surface (left) and in the bottom layer (right) [64]

Рис. 14. Среднее многолетнее распределение солености воды в Обской губе на поверхности (слева) и в придонном слое (справа) [64]

Analysis of the model results and their comparison with the satellite data showed that in some winter seasons the transition zone can shift rather far to the south of the Gulf of Ob, up to the Taz Gulf, i.e., to Site P4 (see Fig. 1, right). Thus, the obtained results confirm the statement of Lapin [63] that in the Gulf of Ob the frontal zone can be observed as far south as 69°N.

It should be noted that the SMOS cell has a size of 15×15 km [68], and the MIRAS pixel size is about 35×65 km [85]. Thus, for some study sites in the Gulf of Ob the MIRAS pixel size exceeds the size of the water area where this site is located. Because of this, some shore area is captured into a MIRAS pixel and that is reflected in brightness temperature, especially in summer (when there is no ice cover). This concerns sites P5-P11 (see Fig. 1, right). In summer, when snow and ice melt away, the emissivities of open water and the shore (tundra and forest vegetation, open soil, marshes) are very different. In winter, the radiative properties of frozen land surface and ice cover are close to each other [80, 86]. Therefore, for sites P6, P8, and P10 (see Figs. 10–12) during open water, the model brightness temperature is slightly lower than that derived from the satellite data.

Analysis of hydrological and meteorological data

The displacement of the transition zone in the Gulf of Ob is influenced by a large number of factors: river runoff, tidal and storm surge phenomena [64] as well as the effects of permafrost thaw in the watershed caused by climate changes [65, 87]. In the northern part of the gulf (sites P7–P13) under-ice water salinity is mostly determined by the influence of the Kara Sea, tidal and storm surge phenomena [64]. The southern part of the gulf (sites P1–P3) is more influenced by the river flows, first of all, of the Ob. On the south of the gulf, the influence of tides and storm surges is insignificant [64]. The central part of the Gulf of Ob (sites P4–P6) is exposed, even during one winter season, to all of the above impacts. Studies [16, 20, 63, 64, 84] show that during winter,

against the background of low river flow, a gradual increase in salinity and mineralization of organic matter in the northern Gulf of Ob is observed. Here, during the autumn low-water period, the influence of seawater intensifies. This causes an increase in salinity of the upper water layers up to 8–9‰ and bottom layers up to 20–22‰ [16, 20, 63, 64]. During winter, the northern Gulf of Ob (north of 71.5°N, Site P10) is subject to an even greater increase in salinity associated with a significant decrease in river runoff (see Figs. 3, 14) and sea bottom currents and tides [20, 64].

Since the Ob River supplies most of the river inflow to the gulf (75–76%), an analysis of climate characteristics along the whole of its length was performed for the study period (2012–2018), and also annual and winter river runoffs for the period from 2011 to 2018 were calculated. Figure 15 shows the dynamics of air temperature, precipitation, and snow cover height plotted using data from 9 weather stations located in different natural climate zones along the Ob (see Table 3). The values of annual runoff of the Ob River near Salekhard are given in Table 4. Table 5 gives the values of annual winter runoff (calculated for the period from November 1 till April 30), annual runoff (calculated for the period from May 1 till April 30), and their percentage ratio.

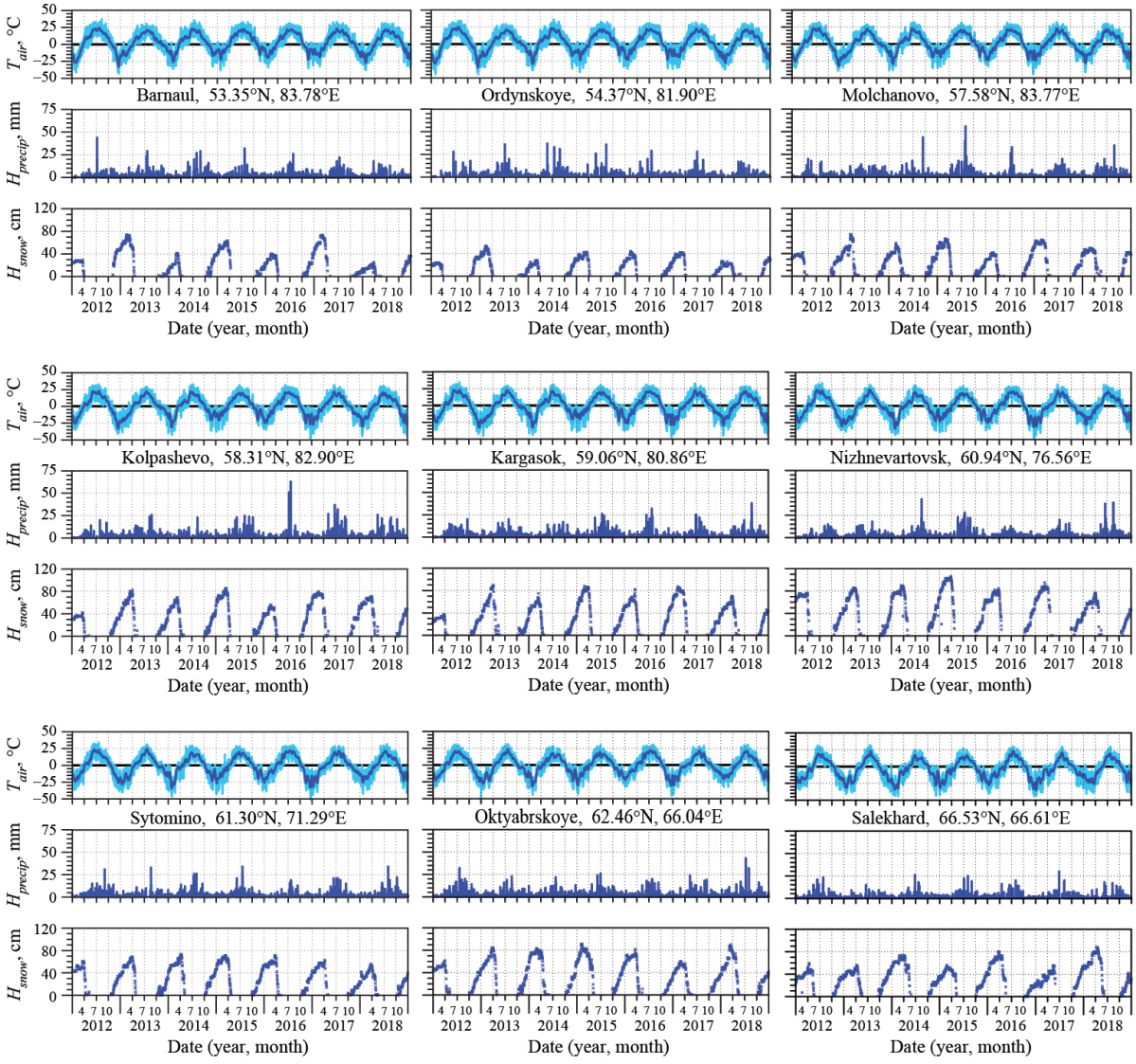

Fig. 15. Air temperature, precipitation, and snow cover height along the Ob River based on data from weather stations (Table 3). Top: Upper Ob, center: Middle Ob, bottom: Lower Ob

Рис. 15. Температура воздуха, количество осадков и высота снежного покрова вдоль реки Обь по данным метеостанций (табл. 3). Вверху: Верхняя Обь, в центре: Средняя Обь, внизу: Нижняя Обь

Table 4

Annual runoff of the Ob River near Salekhard

Таблица 4

Годовой сток реки Обь в районе Салехарда

Year	Annual runoff, km³
2011	405.29
2012	301.14
2013	374.20
2014	480.05
2015	543.24
2016	463.33
2017	456.81
2018	434.91

Table 5

Runoff of the Ob River near Salekhard: winter (November 1 – April 30), annual (May 1 – April 30) and their percentage ratio

Таблица 5

Сток реки Обь у г. Салехард: зимний (1 ноября - 30 апреля), годовой (1 мая - 30 апреля) и их процентное соотношение

Season	Winter, km³	Annual, km³	Winter/Annual, %
2011–2012	84.62	398.18	21
2012–2013	69.56	290.49	24
2013–2014	99.39	391.47	25
2014–2015	111.18	486.82	23
2015–2016	127.80	554.76	23
2016–2017	93.30	448.24	21
2017–2018	88.37	450.00	20

The watershed of the Ob River extends for a great distance from north to south and has a vast area, which determines the diversity of flow formation conditions. Bulavina [66] showed that more than 80% of the Ob runoff is formed in its upper and middle reaches. Lower, it is fed by small tributaries that all make about 5% of the Ob runoff. Thus, the runoff fluctuation patterns are primarily determined by the interaction and overlapping of climate fluctuations in the watersheds of large tributaries of the Upper and Middle Ob. The analysis of Fig. 15 and Table 4 confirms the conclusions of Bulavina [66]. The greatest Ob runoff was observed in 2014, 2015, 2016, and 2017 (see Table 4). These years are characterized, in their warm half, by most intense precipitation in the upper and middle reaches of the river (see Fig. 15). Intense precipitation of the warm half of 2015, the most water plentiful year, was preceded by a large amount of solid precipitation in the cold season (see Section 3.4). Table 5 presents calculations of annual winter runoff of the Ob near Salekhard. The winter runoff does not change much from year to year. It is determined

by the runoff of the whole year and the percentage ratio of winter runoff to annual runoff remains practically the same.

The interannual climate characteristics of the study area and the dynamics of hydrological parameters of the Ob River were found to have no correlation with the satellite data and the model results (compare Figs. 9–12, Fig. 15 and Tables 4, 5). This conclusion is partly supported by Stanovoy [84] who notes a significant interannual variability of surface water salinity in the Ob Gulf in winter (January-April) that is weakly related to the Ob runoff. The same work indicates a much greater relationship between water salinity and the interannual variability of atmospheric processes over the Kara Sea in February.

Table 6

Mean annual air temperature in the area of the Gulf of Ob (Fig. 1, Table 2), °C

Таблица 6

Среднегодовая температура воздуха в районе Обской губы (рис. 1, табл. 2), °C

Weather station	2011	2012	2013	2014	2015	2016	2017	2018
Nyda M	–3.8	–3.9	–6.5	–7.0	–4.9	–3.4	–4.3	–6.0
Novy Port MH	–4.8	–4.8	–7.4	–7.9	–5.9	–4.3	–5.4	–6.8
Antipayuta M	–5.6	–6.5	–9.0	–9.4	–7.1	–5.8	–6.8	–8.1
Seyakha HS	–5.6	–5.9	–9.0	–9.3	–7.0	–5.5	–6.5	–7.6
Imeni Popova St. MH	–5.6	–5.6	–9.4	–9.1	–7.3	–6.0	–6.7	–7.8

Table 6 presents mean annual air temperatures for each year under consideration, obtained at M, MH and HS in the region of the Gulf of Ob (see Table 2). Here, we can see a correspondence of the warmest years (2011, 2012, 2016, 2017) and the minimums of under-ice water salinity for sites P4-P6 in 2012 and 2017 (compare Table 6 and Figs. 9–10). And the salinity minimum is more pronounced by the second warmest year in a row. It should be noted that the maximums of salinity for sites P4-P6 are observed in 2014 and 2015. They are preceded by two coldest years, 2013 and 2014, and also 2015 is a rather cold year (compare Table 6 and Figs. 9–10). This is likely due to the effects of permafrost thaw on Yamal and Gydan peninsulas in warmer years. Permafrost thaw adds fresh water inflow to the Gulf of Ob. Similar processes have been observed recently throughout the Arctic [4, 6, 87-90]. The entire southern and central part of the Gulf of Ob, including the Taz Bay (see Figs. 1), is surrounded by areas of moderate to warm permafrost. The mean annual ground temperature at the depth of the zero annual amplitude varies from 0 to –5 °C, and the thickness of the active layer ranges from 60 to 150 cm [91]. Hence, even a slight increase in the mean annual air temperature may lead to permafrost thaw around the Gulf of Ob and an inflow of freshwater into the Gulf of Ob.

In the northern (P7–P13) and southern (P1–P3) parts of the Gulf of Ob, no dependence of changes in under-ice water salinity on the mean annual air temperature is observed. In the northern part (P7–P13), the Kara Sea waters have the fundamental influence on water salinity; whereas in the southern part (P1–P3), such is the influence of the Ob River runoff [16, 20, 63, 64].

The analysis of hydrological and climate characteristics of the study area showed that during the freezing period, the displacement of the transition zone in the Gulf of Ob is influenced by a complex of factors. Among them, there are climate variations in the region and the Ob River watershed as well as storm surge and tidal phenomena in the Kara Sea and its internal currents.

CONCLUSIONS

Warming of the Arctic entails hydrological and climate changes that are manifested in shrinking ice cover, intense melt of glaciers, reduction in the number and total area of thermokarst lakes, earlier thaw onset and later freeze-up of tundra. Monitoring of hydrological and climate characteristics of the Arctic region has shown that the observed changes are associated with variation in precipitation and temperature fluctuations, degradation of permafrost and tundra vegetation, increased evaporation rates, additional amounts of water vapor and methane entering the atmosphere. The Arctic is attracting attention not only because of climate change, but also because of growing development of large oil and gas fields and consequent aggravation of environmental problems in the region. Operational information about hydrological responses to climate and environmental changes in the Arctic region can be obtained using remote sensing methods.

This article analyzes the seasonal and interannual dependencies of brightness temperature derived from SMOS MIRAS data for different regions of the Gulf of Ob during the freezing period. The analysis is based on comparison of satellite data and model calculations as well as climate characteristics of the area and hydrological parameters of the Gulf of Ob and the Ob River.

It was shown that during winter seasons, the transition zone, the region where fresh and salt waters mix in the Gulf of Ob, can shift as far south as the Taz Bay. The obtained results agree well with the data of Lapin [63] and Voynov et al. [64]. Winter shift of the transition zone depends on a complex of factors: permafrost thaw in the environs of the gulf, river runoff and the influence of the Kara Sea. Variations in these factors are determined by climate changes in the region. However, these results require further confirmation and development.

Note that winter displacement of the transition zone far to the south of the gulf may cause serious and irreversible disturbances to the regional ecosystem. This is due to the fact that the mouth area of the Ob plays a principal role in the reproduction of semi-anadromous fish - sturgeon, peled, muksun, broad whitefish, Siberian whitefish, European whitefish and dogfish. It is the main, unique and the most populated whitefish habitat. The southern and central regions of the Gulf of Ob serve as a wintering area for these fish. Semi-anadromous fish of the Ob River are mostly freshwater forms and cannot withstand increased salinity. Their wintering area in the gulf is constrained on the north by the moving boundary of the transition zone [63]. This fact calls for continuous remote monitoring of this region as well as further investigation into the causes of variations in the hydrological regime of the Gulf of Ob.

Acknowledgments. *The authors express their sincere gratitude to Yu.I. Prilepsky, Head of Novy Port MH of the Northern Agency for Hydrometeorology and Environmental Monitoring (Northern AHEM of Roshydromet), for providing data on the characteristics of ice and snow cover in the Gulf of Ob. The authors thank Tatiana Bocharova (Space Research Institute, Russian Academy of Sciences) for translating the manuscript into English.*

Благодарности. *Авторы выражают искреннюю благодарность Ю. И. Прилепскому, начальнику Морской гидрометеорологической станции "Новый Порт" Северного агентства по гидрометеорологии и мониторингу окружающей среды (Северное УГМС Росгидромета), за предоставленные данные по характеристикам ледового и снежного покрова в Обской губе. Авторы благодарят Т. Ю. Бочарову (Институт космических исследований РАН) за перевод рукописи на английский язык.*

References:

1. Barry R. G., Gan T. Y. The Global Cryosphere. Past, Present, and Future. Cambridge University Press, 2011: 472 p. https://doi.org/10.1017/CBO9780511977947.
2. Day J. W., Rybczyk J. M. Global Change Impacts on the Future of Coastal Systems: Perverse Interactions Among Climate Change, Ecosystem Degradation, Energy Scarcity, and Population, in: Wolanski E., Day J. W. Elliott M., Ramachandran R. (Eds.), Coasts and Estuaries. The Future. Amsterdam: Elsevier, 2019: 621–639. https://doi.org/10.1016/B978-0-12-814003-1.00036-8.
3. Forbes D. L. Arctic Deltas and Estuaries: A Canadian Perspective, in: Wolanski E., Day J. W. Elliott M., Ramachandran R. (Eds.), Coasts and Estuaries. The Future. Amsterdam: Elsevier, 2019: 123–147. https://doi.org/10.1016/B978-0-12-814003-1.00008-3.
4. Jacques J.-M. St., Sauchyn D. J. Increasing winter baseflow and mean annual streamflow from possible permafrost thawing in the Northwest Territories, Canada. Geophysical Research Letters. 2009, 36: L01401. doi: 10.1029/2008GL035822.
5. Makarieva O., Nesterova N., Post D. A., Sherstyukov A., Lebedeva L. Warming temperatures are impacting the hydrometeorological regime of Russian rivers in the zone of continuous permafrost. The Cryosphere. 2019, 13: 1635–1659. https://doi.org/10.5194/tc-13-1635-2019.
6. Suzuki K., Matsuo K., Yamazaki D., Ichii K., Iijima Y., Papa F., Yanagi Y., Hiyama T. Hydrological Variability and Changes in the Arctic Circumpolar Tundra and the Three Largest Pan-Arctic River Basins from 2002 to 2016. Remote Sensing. 2018, 10(3): 402. https://doi.org/10.3390/rs10030402.
7. Somers B., Walker, H.J. Arctic Hydrology, in: Wang Y. (Ed.), The Handbook of Natural Resources, Second Edition, Volume 5, Coastal and Marine Environments. CRC Press is an imprint of Taylor & Francis Group, 2020: 169-174.
8. Glaeser B. Human-Nature Relations in Flux: Two Decades of Research in Coastal and Ocean Management, in: Wolanski E., Day J. W. Elliott M., Ramachandran R. (Eds.), Coasts and Estuaries. The Future. Amsterdam: Elsevier, 2019: 641–659. https://doi.org/10.1016/B978-0-12-814003-1.00037-X.
9. Kravtsova V. I., Cherepanova E. V. Dynamics of the Yenisei and Pur River Deltas. Water Resources. 2003, 30(3): 275–282. doi:10.1023/A:1023882129348.
10. Mikhailov V. N. Gidrologiia ust'ev rek: Uchebnik. Hydrology of river mouths: Textbook. Moscow University Press, 1998: 176 p. [In Russia].
11. Gordeev V. V. Trace elements in water, suspended matter and bottom sediments of the Ob and Yenisey estuaries and the Lena Delta and in the adjacent areas of the Kara and Laptev Seas, in: Kassens H., Lisitzin A. P., Thiede J., Polyakova Ye. I., Timokhov L. A., Frolov I. E. (Eds.), System of the Laptev Sea and the Adjacent Arctic Seas: Modern and Past Environments. Moscow University Press, 2009: 202–225. [In Russia].
12. Khlebovich V. V. K biologicheskoi tipologii estuariev Sovetskogo Soiuza. On biological typology of estuaries of the USSR, in: Khlebovich V. V. (Ed.), Gidrobiologicheskie issledovaniia estuariev. Hydro biological investigations of estuaries. Proceedings of The Zoological institute. 1986, 141: 5–16. [In Russia].
13. Nikanorov A. M., Bryzgalo V. A., Kosmenko L. S., Kondakova M. Yu., Reshetnyak O. S. Antropogennaia nagruzka na ust'ia rek Rossiiskoi Arktiki. Anthropogenic impact on estuaries of the Russian Arctic rivers, in: Kotlyakov V. M., (Ed.), Poliarnaia kriosfera i vody sushi. Polar Cryosphere and Continental Waters. Moscow, Saint-Petersburg: Paulsen Editions, 2011: 288–304. [In Russia].
14. Drits A. V., Arashkevich E. G., Nedospasov A. A., Amelina A. B., Flint M. V. Structural and Functional Characteristics of Zooplankton in the Ob Estuary and Adjacent Shelf Areas of the Kara Sea in Summer. Oceanology. 2019, 59(3): 347–357. doi: 10.31857/S0030-1574593383-395.
15. Galkin S. V., Kucheruk N. V., Minin K. V., Rayskiy A. K., Goroslavskaya E. I. Macrobenthos of the Ob River Estuarine Zone and of the Adjacent Regions of the Kara Sea. Oceanology. 2010, 50(5): 793–797. doi: 10.1134/S0001437010050152.
16. Lapin S. A. Hydrological Characterization of the Ob' Inlet in the Summer and Autumn Seasons. Oceanology. 2011, 51(6): 984–993. doi:10.3390/rs11070835.
17. Lisitsyn A. P., Shevchenko V. P., Vinogradov M. E., Severina O. V., Vavilova V. V., Mitskevich I. N. Particle fluxes in the Kara Sea and Ob and Yenisey estuaries. Oceanology. 1995, 34(5): 683–693.
18. Knizhnikov A. Yu., Golubchikov S. N., Zaitseva Yu. B. Vozmozhnye ekologicheskie posledstviia realizatsii proekta «Iamal-SPG». Possible environmental consequences of the Yamal-LNG project. Energiia: ekonomika, tekhnika, ekologiia. Energy: economics, technology, ecology. 2013, 12: 35–39. [In Russia].

19. Kruk M. N. Ekonomicheskaia otsenka riskov proekta osvoeniia morskikh gazovykh mestorozhdenii Obskoi Guby. Economic development project risk assessment of offshore gas fields Ob bay. Neftegazovoe delo. Oil and gas business. 2012, 1: 230–242. [In Russia]. Available at: http://ogbus.ru/article/view/ekonomicheskaya-ocenka-riskov-proekta-osvoeniya-morskix-gazovyx-mestorozhdenij-obskoj-guby
20. Ilyin G. V. Gidrologicheskii rezhim Obskoi guby kak novoi oblasti morskogo prirodopol'zovaniia v rossiiskoi Arktike. Hydrological conditions of the Ob bay as new area of maritime wildlife management in the Russian Arctic. Nauka iuga Rossii. Science in the south of Russia. 2018, 14(2): 20-32. [In Russia]. doi: 10.23885/2500-0640-2018-14-2-20-32.
21. Gens R. Remote Sensing of Coastlines: Detection, Extraction and Monitoring. International Journal of Remote Sensing. 2010, 31(7): 1819–1836. https://doi.org/10.1080/01431160902926673.
22. Khorram S. Remote Sensing of Salinity in the San Francisco Bay Delta. Remote Sensing of Environment. 1982, 12(1): 15–22. https://doi.org/10.1016/0034-4257(82)90004-9.
23. Klemas V. V. Sensors and Techniques for Observing Coastal Ecosystems, in: Yang, X. (Ed.), Remote Sensing and Geospatial Technologies for Coastal Ecosystem Assessment and Management. Berlin: Springer, 2009: 17–44. doi: 10.1007/978-3-540-88183-4_2.
24. Kuenzer C., Heimhuber V., Huth J., Dech S. Remote Sensing for the Quantification of Land Surface Dynamics in Large River Delta Regions — A Review. Remote Sensing. 2019, 11(17): 1985. doi https://doi.org/10.3390/rs11171985.
25. Yang X. Remote Sensing, Geospatial Technologies and Coastal Ecosystems, in: Yang, X. (Ed.), Remote Sensing and Geospatial Technologies for Coastal Ecosystem Assessment and Management. Berlin: Springer, 2009: 1–14. doi: 10.1007/978-3-540-88183-4_1.
26. Cui B., Li X. Y. Coastline Change of the Yellow River Estuary and Its Response to the Sediment and Runoff (1976–2005). Geomorphology. 2011, 127: 32–40. https://doi.org/10.1016/j.geomorph.2010.12.001.
27. Fan H., Huang H., Zeng T. Q. Wang K. River Mouth Bar Formation, Riverbed Aggradation and Channel Migration in the Modern Huanghe (Yellow) River Delta, China. Geomorphology. 2006, 74: 124–136. https://doi.org/10.1016/j.geomorph.2005.08.015.
28. Li X., Damen M. Coastline Change Detection with Satellite Remote Sensing for Environmental Management of the Pearl River Estuary, China. Journal of Marine Systems. 2010, 82: 54–61. doi: 10.1016/j.jmarsys.2010.02.005.
29. Liu H. Shoreline Mapping and Coastal Change Studies Using Remote Sensing Imagery and LIDAR Data, in: Yang, X. (Ed.), Remote Sensing and Geospatial Technologies for Coastal Ecosystem Assessment and Management. Berlin: Springer, 2009: 297–322. doi: 10.1007/978-3-540-88183-4_13.
30. Petropoulos G. P., Kalivas D. P., Griffiths H. M., Dimou P. P. Remote Sensing and GIS Analysis for Mapping Spatio-Temporal Changes of Erosion and Deposition of Two Mediterranean River Deltas: The Case of the Axios and Aliakmonas Rivers, Greece. International Journal of Applied Earth Observation and Geoinformation. 2015, 35: 217–228. https://doi.org/10.1016/j.jag.2014.08.004.
31. Hori M. Near-daily monitoring of surface temperature and channel width of the six largest Arctic rivers from space using GCOM-C/SGLI. Remote Sensing of Environment. 2021, 263: 112538. https://doi.org/10.1016/j.rse.2021.112538.
32. Pavelsky T. M., Smith L. C. Spatial and Temporal Patterns in Arctic River Ice Breakup Observed with MODIS and AVHRR Time Series. Remote Sensing of Environment. 2004, 93(3): 328–338. https://doi.org/10.1016/j.rse.2004.07.018.
33. Klok L., van Harmelen T., Janssen S. Urban Heat and Heat Stress in Rotterdam. Proceedings of the Deltas in Times of Climate Change. International Conference. Rotterdam, The Netherlands, 29 September – 1 October 2010. 2010: 141–142.
34. Antonova S., Kääb A., Heim B., Langer M., Boike J. Spatio-temporal variability of X-band radar backscatter and coherence over the Lena River Delta, Siberia. Remote Sensing of Environment. 2016, 182: 169–191. https://doi.org/10.1016/j.rse.2016.05.003.
35. Grings F., Salvia M., Karszenbaum H., Ferrazzoli P., Kandus P., Perna P. Exploring the Capacity of Radar Remote Sensing to Estimate Wetland Marshes Water Storage. Journal of Environmental Management. 2008, 90: 2189–2198. https://doi.org/10.1016/j.jenvman.2007.06.029.
36. Omari K., Chenier R., Touzi R., Sagram M. Investigation of C-Band SAR Polarimetry for Mapping a High-Tidal Coastal Environment in Northern Canada. Remote Sensing. 2020, 12(12): 1941. https://doi.org/10.3390/rs12121941.
37. Ottinger M., Kuenzer C. Spaceborne L-Band Synthetic Aperture Radar Data for Geoscientific Analyses in Coastal Land Applications: A Review. Remote Sensing. 2020, 12(14): 2228. https://doi.org/10.3390/rs12142228.

38. Syvitski J. P. M., Overeem I., Brakenridge G. R., Hannon M. Floods, Floodplains, Delta Plains - A Satellite Imaging Approach. Sedimentary Geology. 2012, 267–268: 1–14. https://doi.org/10.1016/j.sedgeo.2012.05.014.
39. Abascal-Zorrilla N., Vantrepotte V., Huybrechts N., Ngoc D. D., Anthony E. J., Gardel A. Dynamics of the Estuarine Turbidity Maximum Zone from Landsat-8 Data: The Case of the Maroni River Estuary, French Guiana. Remote Sensing. 2020, 12: 2173. https://doi.org/10.3390/rs12132173.
40. Baban S. M. J. Detecting water quality parameters in the Norfolk Broads, U.K., using Landsat imagery. International Journal of Remote Sensing. 1993, 14(7): 1247-1267. doi: 10.1080/01431169308953955.
41. Lavrova O. Y., Soloviev D. M., Mityagina M. I., Strochkov A. Y., Bocharova T. Y. Revealing the influence of various factors on concentration and spatial distribution of suspended matter based on remote sensing data. Proceedings of the Remote Sensing of the Ocean, Sea Ice, Coastal Waters, and Large Water Regions 2015, Toulouse, France, 21–24 September 2015. SPIE — International Society for Optics and Photonics, Bellingham. 2015, 9638: 96380D. doi: 10.1117/12.2193905.
42. Lavrova O. Y., Soloviev D. M., Strochkov M. A., Bocharova T. Y., Kashnitsky A. V. River plumes investigation using Sentinel-2A MSI and Landsat-8 OLI data. Proceedings of the Remote Sensing of the Ocean, Sea Ice, Coastal Waters, and Large Water Regions 2016, Edinburgh, UK, 26–29 September 2016. SPIE — International Society for Optics and Photonics, Bellingham. 2016, 9999: 99990G. doi: 10.1117/12.2241312.
43. Nazirova K., Lavrova O., Krayushkin E. Features of monitoring near the mouth zones by contact and contactless methods. Proceedings of the Remote Sensing of the Ocean, Sea Ice, Coastal Waters, and Large Water Regions 2019, Strasbourg, France, 9–12 September 2019. SPIE — International Society for Optics and Photonics, Bellingham. 2019, 11150: 111500H. https://doi.org/10.1117/12.2533165.
44. Nazirova K., Alferyeva Y., Lavrova O., Shur Y., Soloviev D., Bocharova T., Strochkov A. Comparison of In Situ and Remote-Sensing Methods to Determine Turbidity and Concentration of Suspended Matter in the Estuary Zone of the Mzymta River, Black Sea. Remote Sensing. 2021, 13: 143. https://doi.org/10.3390/rs13010143.
45. Ray R., Mandal S., Dhara A. Environmental monitoring of estuaries: Estimating and mapping various environmental indicators in Matla estuarine complex, using Landsat TM digital data. Intern. J. Geomatics and Geosciences. 2013, 3(3): 570–581.
46. Tarpanelli A., Iodice F., Brocca L., Restano M., Benveniste J. River Flow Monitoring by Sentinel-3 OLCI and MODIS: Comparison and Combination. Remote Sensing. 2020, 12: 3867. https://doi.org/10.3390/rs12233867.
47. Wei Z., Jia K., Liu P., Jia X., Xie Y., Jiang Z. Large-Scale River Mapping Using Contrastive Learning and Multi-Source Satellite Imagery. Remote Sensing. 2021, 13(15): 2893. https://doi.org/10.3390/rs13152893.
48. Tedesco M. Remote sensing of the Cryosphere. Oxford: JohnWiley & Sons, 2015. 404 p. doi: 10.1002/9781118368909.
49. Akimov D. B., Johannessen O. M., Mitnik L. M., Volkov V. A. Satellite radar signatures of fronts in the Ob and Yenisey estuaries in the Kara Sea. Proceedings IEEE International Geoscience and Remote Sensing Symposium, IGARSS'99. 1999, 5: 2542–2544. doi: 10.1109/IGARSS.1999.771570.
50. Melentyev V. V., Johannessen O. M, Sandven S., Pettersson L. H. Ice Regime Study for the Ob-Yenisey Estuaries Using ERS SAR Data. Proceedings IEEE International Geoscience and Remote Sensing Symposium, IGARSS'99. 1999, 2: 1037–1039. doi: 10.1109/IGARSS.1999.774525.
51. Melentyev V., Bobylev L., Pettersson L., Sandven S. Winter hydrology and ice regime of the Ob – Yenisey estuaries: results of satellite SAR comprehensive studies. Proceedings 31st International Symposium on Remote Sensing of Environment (ISRSE), Saint Petersburg, 20–24 May. 2005.
52. Sharkov E. A. Passive Microwave Remote Sensing of the Earth: Physical Foundations. Berlin: Springer/PRAXIS, 2003. 656 p.
53. Kugler Z., Nghiem S. V., Brakenridge G. R. L-Band Passive Microwave Data from SMOS for River Gauging Observations in Tropical Climates. Remote Sensing. 2019, 11(7): 835. https://doi.org/10.3390/rs11070835.
54. Papa F., Prigent C., Rossow W. B. Monitoring Flood and Discharge Variations in the Large Siberian Rivers from a Multi-Satellite Technique. Surveys in Geophysics. 2008, 29(4): 297-317. doi: 10.1007/s10712-008-9036-0.
55. Stippel S. J., Hamilton S. K., Melack J. M., Choudhury B. J. Determination of inundation area in the Amazon River floodplain using SMMR 37 GHz polarization difference. Remote

Sensing of Environment. 1994, 48: 70-76. https://doi.org/10.1016/0034-4257(94)90115-5.
56. Du J., Kimball J. S., Jones L. A., Watts J. D. Implementation of satellite based fractional water cover indices in the pan-Arctic region using AMSR-E and MODIS. Remote Sensing of Environment. 2016, 184: 469–481. https://doi.org/10.1016/j.rse.2016.07.029.
57. Khan S. I., Hong Y., Vergara H. J., Gourley J. J., Brakenridge G. R., Groeve T. D., Flamig Z. L., Policelli F., Yong B. Microwave Satellite Data for Hydrologic Modeling in Ungauged Basins. IEEE Geoscience and Remote Sensing Letters. 2012, 9(4): 663–667. doi: 10.1109/LGRS.2011.2177807.
58. Temimi M., Leconte R., Brissette F., Chaouch N. Flood monitoring over the Mackenzie River Basin using passive microwave data. Remote Sensing of Environment. 2005, 98: 344–355. https://doi.org/10.1016/j.rse.2005.06.010.
59. Umbert M., Gabarro C., Olmedo E., Gonçalves-Araujo R., Guimbard S., Martinez J. Using Remotely Sensed Sea Surface Salinity and Colored Detrital Matter to Characterize Freshened Surface Layers in the Kara and Laptev Seas during the Ice-Free Season. Remote Sensing. 2021, 13: 3828. https://doi.org/10.3390/rs13193828.
60. Tikhonov V. V., Khvostov I. V., Romanov A. N., Sharkov E. A. Analysis of changes in the ice cover of freshwater lakes by SMOS data. Izvestiya, Atmospheric and Oceanic Physics. 2018, 54(9): 1135–1140. doi: 10.1134/S0001433818090384.
61. Tikhonov V. V., Khvostov I. V., Romanov A. N., Sharkov E. A. Theoretical study of ice cover phenology at large freshwater lakes based on SMOS MIRAS data. The Cryosphere. 2018, 12(8): 2727–2740. doi: 10.5194/tc-12-2727-2018.
62. Tikhonov V. V., Khvostov I. V., Romanov A. N., Sharkov E. A., Boyarskii D. A., Komarova N. Yu., Sinitskiy A. I. Features of the Intrinsic L-Band Radiation of the Gulf of Ob during the Freeze-Up Period. Izvestiya, Atmospheric and Oceanic Physics. 2020, 56(9): 9362–949. doi: 10.1134/S0001433820090236.
63. Lapin S. A. Prostranstvenno-vremennaia izmenchivost' gidrologo-gidrokhimicheskikh kharakteristik Obskoi guby kak osnova otsenki ee bioproduktivnosti. Spatial and temporal variability of the hydro-hydrochemical characteristics of the Ob Bay as a basis for assessing its bioproductivity. PhD thesis. Russian Federal Research Institute of Fisheries and Oceanography. Moscow. 2012: 128 p. [In Russia].
64. Voynov G. N., Nalimov Yu. V., Piskun A. A., Stanovoy V. V., Usankina G. E. Osnovnye cherty gidrologicheskogo rezhima Obskoi i Tazovskoi gub (led, urovni, struktura vod). The main features of the hydrological regime of the Ob and Taz bays (ice, levels, water structure). Saint-Petersburg: Nestor-History, 2017. 192 p. [In Russia].
65. Dolgopolova E. N. Rol' mnogoletnemerzlykh porod v formirovanii gidrologo-morfologicheskogo rezhima ust'ev rek vodosbora Severnogo Ledovitogo okeana. The role of permafrost in the formation of the hydrological and morphological regime of river mouths in the Arctic Ocean watershed area. Arktika: ekologiia i ekonomika. Arctic: Ecology and Economy. 2018, 32(4): 70–85. [In Russian]. doi: 10.25283/2223-4594-2018-4-70-85.
66. Bulavina A. S. Klimaticheskie faktory formirovaniia stoka reki Ob'. Climatic factors of the Ob River runoff formation. Nauka iuga Rossii. Science in the south of Russia. 2020, 16(1): 45–54. [In Russia]. https://doi.org/10.7868/S25000640200106.
67. Gutierrez A., Castro R., Vieira P, Lopes G., Barbosa J. SMOS L1 Processor L1c Data Processing Model. Portugal: DEIMOS Engenharia. 2014.
68. Sahr K., White D., Kimerling A. J. Geodesic Discrete Global Grid System. Cartography and Geographic Information Science. 2003, 30(2): 121-134. https://doi.org/10.1559/152304003100011090.
69. Andreev O. M., Drabenko D. V., Vinogradov R. A., Orlova E. U. Vliianie potepleniia klimata na prochnostnye kharakteristiki l'da v Obskoi gube. Influence of climate warming on the strength characteristics of ice in the Ob Bay. Led i sneg. Ice and Snow. 2019, 59(4): 539–545. [In Russia]. https://doi.org/10.15356/2076-6734-2019-4-409.
70. Tikhonov V. V., Boyarskii D. A., Sharkov E. A., Raev M. D., Repina I. A., Ivanov V. V, Alexeeva T. A., Komarova N. Yu. Microwave Model of Radiation from the Multilayer “Ocean-atmosphere” System for Remote Sensing Studies of the Polar Regions. Progress In Electromagnetics Research B. 2014, 59: 123–133. doi: 10.2528/PIERB14021706.
71. Demir O., Johnson J. T., Jezek K. C., Andrews M. J., Ayotte K., Spreen G., Hendricks S., Kaleschke L., Oggier M., Granskog M. A., Fong A., Hoppmann M., Matero I., Scholz D. Measurements of 540–1740 MHz Brightness Temperatures of Sea Ice During the Winter of the MOSAiC Campaign. IEEE Transactions on Geoscience and Remote Sensing. 2022, 60: 5302011. doi: 10.1109/TGRS.2021.3105360.
72. Boyarskii D. A., Tikhonov V. V., Kleeorin N. I., Mirovskii V. G. Inclusion of scattering losses in the models of the effective permittivity of dielectric mixtures and applications to

wet snow. J. of Electromagnetic Waves and Applications. 1994, 8(11): 1395–1410. doi: 10.1163/156939394X00281.
73. Crabeck O., Galley R., Delille B., Else B., Geilfus N.-X., Lemes M., Roches M. D., Francus P., Tison J.-L., Rysgaard S. Imaging air volume fraction in sea ice using non-destructive X-ray tomography. The Cryosphere. 2016, 10(3): 1125–1145. doi: https://doi.org/10.5194/tc-10-1125-2016.
74. Frantz C. M., Light B., Farley S. M., Carpenter S., Lieblappen R., Courville Z., Orellana M. V., Junge K. Physical and optical characteristics of heavily melted "rotten" Arctic Sea ice. The Cryosphere. 2019, 13: 775–793. doi: https://doi.org/10.5194/tc-13-775-2019.
75. Gray D. M., Male D. H. (Eds.). Handbook of Snow. Toronto: Pergamon Press, 1981. 776 p.
76. Lepparanta M. Freezing of Lakes and the Evolution of their Ice Cover. Chichester: Springer, 2015. 301 p. doi: 10.1007/978-3-642-29081-7.
77. Petrich C., Eicken H. Growth, Structure and Properties of Sea Ice, in: Thomas D. N., Dieckmann G. S. (Eds.), Sea Ice. Second Edition. Chichester: Blackwell Publishing Ltd, 2010: 23–77.
78. Singh V. P., Singh P., Haritashya U. K. (Eds.). Encyclopedia of Snow, Ice and Glaciers. Dordrecht: Springer, 2011. 1253 p. https://doi.org/10.1007/978-90-481-2642-2.
79. Timco G. W., Frederking R. M. W. A review of sea ice density. Cold Regions Science and Technology. 1996, 24: 1–6. https://doi.org/10.1016/0165-232X(95)00007-X.
80. Ulaby F. T., Long D. G. Microwave Radar and Radiometric Remote Sensing. Univ. of Michigan Press, 2014. 984 p.
81. Polukhin A. A., Makkaveev P. N. Features of the Continental Runoff Distribution over the Kara Sea. Oceanology. 2017, 57(1): 19–30. https://doi.org/10.1134/S0001437017010143.
82. Zatsepin A. G., Zavialov P. O., Kremenetskiy V. V., Poyarkov S. G., Soloviev D. M. The Upper Desalinated Layer in the Kara Sea. Oceanology. 2010, 50(5): 657–667. doi: 10.1134/S0001437010050036.
83. Naoki K., Ukita J., Nishio F., Nakayama M., Comiso J. C., Gasiewski A. Thin sea ice thickness as inferred from passive microwave and in situ observations. Journal of Geophysical Research. 2008, 113: C02S16. doi: 10.1029/2007JC004270.
84. Stanovoy V. V. Izmenchivost' termokhalinnoi struktury vody v estuariiakh Karskogo moria. Variability of thermohaline water structure in the Kara Sea estuaries. Trudy Arkticheskogo I antarkticheskogo nauchnoy-issledovatel'skogo instituta. Proceedings of the AARI. 2008, 448: 103–130. [In Russia].
85. Kerr Y. H., Waldteufel P., Wigneron J.-P., Delwart S., Cabot F., Boutin J., Escorihuela M. J., Font J., Reul N., Gruhier C., Juglea S. E., Drinkwater M. R., Hahne A., Martin-Neira M., Mecklenburg S. The SMOS Mission: New Tool for Monitoring Key Elements of the Global Water Cycle. Proceeding of the IEEE. 2010, 98(5): 666–687. doi: 10.1109/JPROC.2010.2043032.
86. Emery W., Camps A. Introduction to Satellite Remote Sensing: Atmosphere, Ocean, Land and Cryosphere Application. Amsterdam: Elsevier Inc, 2017. 856 p. https://doi.org/10.1016/C2015-0-04517-8.
87. Kokelj S. V., Kokoszka J., van der Sluijs J., Rudy A. C. A., Tunnicliffe J., Shakil S., Tank S. E., Zolkos S. Thaw-driven mass wasting couples slopes with downstream systems, and effects propagate through Arctic drainage networks. The Cryosphere. 2021, 15(7): 3059–3081. https://doi.org/10.5194/tc-15-3059-2021.
88. Lin H., Cheng X., Zheng L., Peng X., Feng W., Peng F. Recent Changes in Groundwater and Surface Water in Large Pan-Arctic River Basins. Remote Sensing. 2022, 14(3): 607. https://doi.org/10.3390/rs14030607.
89. Suzuki K., Park H., Makarieva O., Kanamori H., Hori M., Matsuo K., Matsumura S., Nesterova N., Hiyama T. Effect of Permafrost Thawing on Discharge of the Kolyma River, Northeastern Siberia. Remote Sensing. 2021, 13(21): 4389. https://doi.org/10.3390/rs13214389.
90. Walvoord M.A., Kurylyk B.L. Hydrologic Impacts of Thawing Permafrost-A Review. Vadose Zone Journal. 2016, 6(15). https://doi.org/10.2136/vzj2016.01.0010.
91. Ran Y., Li X., Cheng G., Che J., Juha A., Olli K., Jan H., Miska L., Jin H., Jaroslav O., Masahiro H., Yu Q., Chang X. New high-resolution estimates of the permafrost thermal state and hydrothermal conditions over the Northern Hemisphere. Earth System Science Data. 2022, 14: 865–884. https://doi.org/10.5194/essd-14-865-2022.